UNIVERSITY OF CALIFORNIA,
IRVINE

Dark Matter Coupling To Quarks

DISSERTATION

submitted in partial satisfaction of the requirements
for the degree of

DOCTOR OF PHILOSOPHY

in Physics

by

Dillon Berger

Dissertation Committee:
Prof. Arvind Rajaraman, Chair
Prof. Mu-Chun Chen
Prof. Yuri Shirman

2021

DEDICATION

To my mother Barbara Reed, for her unwavering belief in me and unconditional support since the day this journey began.

TABLE OF CONTENTS

LIST OF FIGURES

LIST OF TABLES

ACKNOWLEDGMENTS

The completion of this dissertation would not have been made possible without the open and dedicated community that is the UCI Particle Theory Group. In particular, I would like to thank my advisor Arvind Rajaraman for his guidance to me as a young graduate student, and his persistent honesty and directness which together aided and accelerated my intellectual growth. I would also like to thank Mu-Chun Chen, the first person in the department with whom I worked; as her helpfulness to me as a nascent particle theory student cannot be overstated. I would also like to thank Michael Ratz for his dedication to creating such a thorough and helpful textbook for particle theory students which formed the foundations of my thinking on the subject. Finally I would also like to thank Tim Tait for his lucid lectures on the otherwise-nebulous topic of quantum field theory.

I would like to acknowledge my many collaborators: Seyda Ipek, Michal Waterbury, Tim Tait, Jessica Howard, Jason Kumar and Arvind Rajaraman. I would also like to thank my peer Michael Waterbury for some of the most useful and informative discussions I ever had while at UC Irvine. I would also like to thank Rebecca Riley for her unwavering dedication to help and encourage me in applying for the GRFP fellowship; her help in this regard was truly invaluable. Lastly, I would also like to thank Arianna Braconi for our insightful discussions on thermal quantum field theory, and also for being a great friend.

This work was supported in part by the NSF Graduate Research Fellowship via grant number DGE-1839285, NSF grant PHY-1915005, NSF grant PHY-1620638, and DOE grant DE-SC0010504.

VITA

Dillon Berger

EDUCATION

Doctor of Philosophy in Physics **2021**
University of California, Irvine *Irvine, CA*

Bachelor of Science in Physics **2017**
George Mason University *Fairfax, VA*

Bachelor of Arts in Mathematics **2017**
George Mason University *Fairfax, VA*

Bachelor of Arts in Philosophy **2017**
George Mason University *Fairfax, VA*

RESEARCH EXPERIENCE

NSF Research Fellow **2019–2021**
University of California, Irvine *Irvine, CA*

Graduate Research Assistant **2017–2019**
University of California, Irvine *Irvine, CA*

TEACHING EXPERIENCE

Graduate Teaching Assistant **2017–2019**
University of California, Irvine *Irvine, CA*

REFEREED JOURNAL PUBLICATIONS

Invariant Tensors in Gauge Theories **2018**
Letters in High Energy Physics

Dark Matter Through The Quark Vector Current Portal **2018**
Pramana

Dark Matter Freeze Out during an Early Cosmological Period of QCD Confinement **2020**
Journal of High Energy Physics

Dark Matter Through The Quark Axial-Vector Current Portal **2021**
To appear

ABSTRACT OF THE DISSERTATION

Dark Matter Coupling To Quarks

By

Dillon Berger

Doctor of Philosophy in Physics

University of California, Irvine, 2021

Prof. Arvind Rajaraman, Chair

The primary focus of this work is to explore the implications of dark matter models in which dark matter is light ($\lesssim \mathcal{O}(\text{GeV})$) and interacts with the standard model quarks. In Chapter 2 we consider dark matter coupling to the quarks as a vector current interaction for two distinct cases. In the first case we take dark matter to be a new spin-1 vector particle which decays into standard model particles, and in the second case we take dark matter to be a Dirac fermion which annihilates into standard model final states. We then impose constraints on these models by comparing the resulting photon signatures of dark matter annihilation/decay to the background diffuse emission and to future observations of the dwarf spheroidal galaxy Draco. Similarly, in Chapter 3 we again consider dark matter as a sub-GeV Dirac fermion and impose model constraints by examining its photon signature that results from the decay of its standard model final states. However, in this case we take the method of dark matter communication to the standard model to be through an axial-vector interaction (as opposed to a vector-like current). In both cases, we obtain constraints on the models by comparing the estimated photon signals to current and future observations, and show that the axial-vector DM portal is significantly more conducive to photon production for lighter forms of dark matter than a pure vector-like portal; establishing itself as a prime candidate for indirect detection probes with significant discovery reach.

Then in Chapter 4 we slightly change gears by considering dark matter coupling to quarks in the early universe. We explore a nonstandard cosmology in which the strong coupling constant evolves in the early Universe, triggering an early period of QCD confinement at the time of dark matter freeze out. We find that depending on the nature of the interactions between the dark matter and the Standard Model, freeze out during an early period of confinement can lead to drastically different expectations for the relic density, allowing for regions of parameter space which realize the correct abundance but would otherwise be excluded by direct searches.

Chapter 1

Introduction

1.1 The Standard Model

The Standard Model (SM) provides a unified picture of the electroweak (EW) and strong interactions, and prescribes different "charges" to the most fundamental particles we know of. These fundamental particles are split into 2 categories: Fermions, which carry half-integer spin, and Bosons, which carry integer spin. The fermions are further split into two categories, each of which consists of three 'families' (or 'generations'): (1) The quarks, which carry fractional electric charge, and (2) the leptons which carry integer electric charge. There are 4 gauge bosons, which mediate the fundamental forces: There's gluon and the photon which are both massless and mediate the strong interaction and electromagnetic force respectfully. Then there are the $W^{\pm}$ and Z bosons which are massive gauge fields and mediate the weak interaction. The final ingredient to the standard model is the Higgs field, which is a spin-0 scalar field and is responsible for the spontaneous breaking of the $SU(2)_L \times U(1)_Y$ electroweak symmetry and consequently generating the masses of the fermions and electroweak bosons.

More formally, the Standard Model is a Lorentz invariant chiral gauge theory based on the

SM gauge group

$$G_{SM} = SU(3)_c \times SU(2)_L \times U(1)_Y. \tag{1.1}$$

The representations we assign to the particle content are of the fundamental ingredients of the SM. All of the Standard Model Fermions (along with the Higgs), are shown in Table 1.1 next to their corresponding representations under G_{SM}.

Particle	Representation
$\begin{pmatrix} \nu_i \\ e_i \end{pmatrix}_L$	$(\mathbf{1}, \mathbf{2})_{-1/2}$
$\begin{pmatrix} u_i \\ d_i \end{pmatrix}_L$	$(\mathbf{3}, \mathbf{2})_{1/6}$
$e_R^{(i)}$	$(\mathbf{1}, \mathbf{1})_{-1}$
$u_R^{(i)}$	$(\mathbf{3}, \mathbf{1})_{2/3}$
$d_R^{(i)}$	$(\mathbf{3}, \mathbf{1})_{-1/3}$
h	$(\mathbf{1}, \mathbf{2})_{1/2}$

Table 1.1: All of the Standard Model fundamental particles and their associated representations under $SU(3)_c \times SU(2)_L \times U(1)_Y$

In addition to the particle content shown in Table 1.1, we note that all of the SM gauge fields transform in the adjoint representation of their corresponding gauge groupsand have hypercharge $Y = 0$.

1.1.1 Standard Model Shortcomings

Now, despite the many successes of the Standard model, there's still a number of open questions. For a good overview and description of the the current open problems in the

Standard Model see [72]. In this work, however, we focus our time mainly on discussing the problem of dark matter (DM). In short, the problem of dark matter can be summarized as follows: There are multiple avenues of indirect evidence (see Section 1.2.1) which indicate that there must be more matter in the universe that we can visibly see. More than that, not only can we not 'see' this extra matter, but it also doesn't appear to interact with any of the forces other than gravity (or if it does it must do so very weakly). This inability to strongly interact with anything other than gravity is directly responsible for what makes dark matter so elusive in the pursuit of direct detection. We dedicate Section 1.2.1 to making these statements more precise; giving a brief overview of the relevant background and going over some of the evidence for dark matter.

1.2 Dark Matter Overview

1.2.1 Background and Evidence

Let us start by briefly going over some of the evidence for dark matter, the first of which we'll talk about is the galaxy rotation curves shown in Figure 1.1.

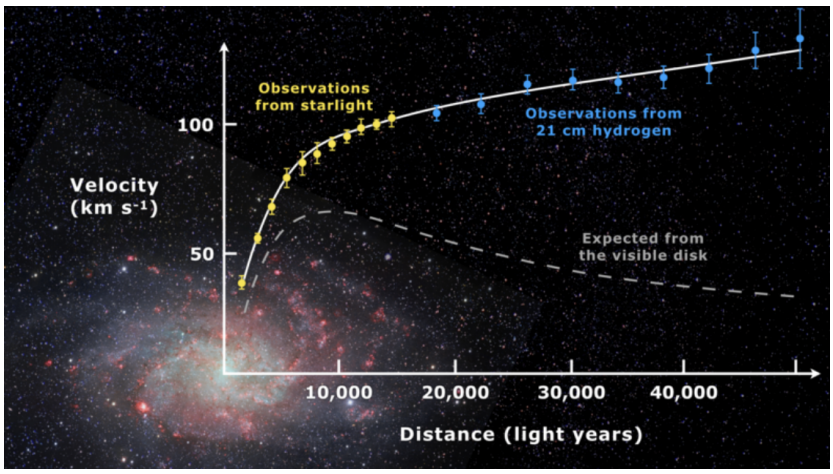

Figure 1.1: The lower curve is the galaxy rotation curve expected from the visible matter in the galaxy, and the upper curve is the observed galaxy rotation curve.

On this plot, we have the average orbital speed of visible stars and gas (i.e. "visible matter") in the galaxy as a function of the radial distance from the galactic center. The dotted line is the rotation curve that would be expected if the visible matter were all the matter in the galaxy, with the rotational velocities decreasing with distance from the central galactic bulge. However, the solid is the observed rotation curve form visible matter. The visible matter is measured by starlight and galactic dust (in yellow) until about 18×10^3 light years, after which point the starlight becomes too faint and the matter is estimated from 21 cm hydrogen (in blue).

There is a very clear discrepancy in the expected and observed rotation curves, which is most prominent in the behavior far from the galactic bulge. Heuristically, what this is saying is that the galaxy is spinning too fast to be stable and that it should instead be flying apart. So there must be "extra matter" there that we can't see holding it together. Said more quantitatively, Newtonian mechanics tells us that the rotational velocity v goes as

$$v^2(r) = Gr\frac{d}{dr}\int \mathrm{d}^3 r \ \frac{\rho(r)}{r} \tag{1.2}$$

and so the rotation curve can only vary with with the mass density $\rho(r)$. Hence in order to fit the observed rotation curve we need to account for missing terms in the density function ρ, which translates physically that we need to account for missing matter. This "missing matter" was dubbed dark matter.

Next we consider the dark matter evidence known as the bullet cluster (Figure 1.2), which is the result of a collision of two galaxies.

The blue region in this figure indicates the regions where gravity is strongest, which is found my measuring the amount of gravitational lensing. The brightness of the blue corresponds

Figure 1.2: Bullet cluster gravitational lensing map (brightness proportional to lensing strength). The pink region is lensing strength from visible matter, and blue region is lensing strength from a non-luminous source.

to the strength of the lensing. The pink region shows the x-ray data associated with the gas clouds, and so depicts the distribution of the regular baryonic matter (i.e. "visible matter"). The main takeaway of this result is that there's a clear separation between the x-ray and gravitational lensing maps in the bullet cluster. Most noticeably, the regions where the gravitational lensing is the strongest appear to actually have very little baryonic matter. Moreover, note that the galaxy collision distorts the shape of the region containing baryonic region, whereas the regions with the strongest gravitational lensing maintain their roughly spherical initial shape they had prior to the collision. All of this taken together is indicative of a collision-less non-baryonic halo surrounding the galaxies

1.2.2 Direct Vs. Indirect Detection

We now move to an overview of the different methods one can use to detect particle dark matter. Dark matter detection methods can roughly be categorized into three separate classes, two of which we'll discuss here: (1) direct detection and (2) indirect detection of dark matter. The method that we've not mentioned is collider searches for dark matter,

which is smashing two SMs to create a DM particle.

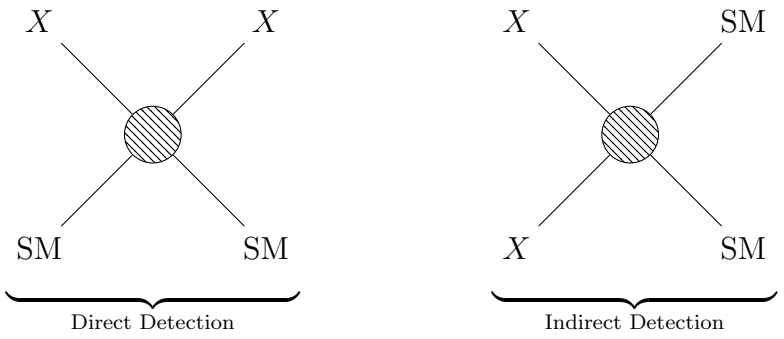

(1.3)

In brief, direct dark matter detection attempts to measure the scattering of a dark matter particle off of a Standard Model particle, usually by measuring the recoil energies of atomic nuclei. Direct detection of lighter forms of dark matter ($\lesssim 1$ GeV) is notoriously difficult. This is because dark matter interacts very weakly (if at all) with the standard model and so its scattering off a nucleus produces extremely small recoil energies. To detect these minuscule recoils of atomic nuclei of $\sim$ GeV dark matter requires a sensitivity on the scale of 10^{-49} cm^2 [73], as well as an extremely low background. The experimental difficulties only increase with decreasing dark matter mass, and so for these reasons direct detection is only realistically useful for probing dark matter candidates with masses above this GeV threshold.

More precisely, in direct detection the measured quantity is the is the event rate of nuclear recoils, which is a function of only two unknowns: the DM mass and the DM-nucleus scattering cross section. So for a given observed event rate (or lower bound) there is a curve of all the masses and cross sections consistent with that observation in parameter space. If no events are detected then this curve provides an upper bound on the dark matter scattering cross section as a function of the dark matter mass. In Figure 1.3 we have shown a collection of the results of all dark matter direct detection experiments from 2016 through 2019.

The other method of detection is the indirect detection of dark matter, wherein one attempts to measure the process of dark matter particles annihilating or decaying into standard model final states. Contrary to direct detection methods, indirect detection is sensitive to dark matter regardless of its mass, and so is accommodating to dark matter below the GeV threshold. The price we pay for this accommodating nature of indirect detection however is that most of the bounds obtained from indirect probes are less constraining and usually model dependent.

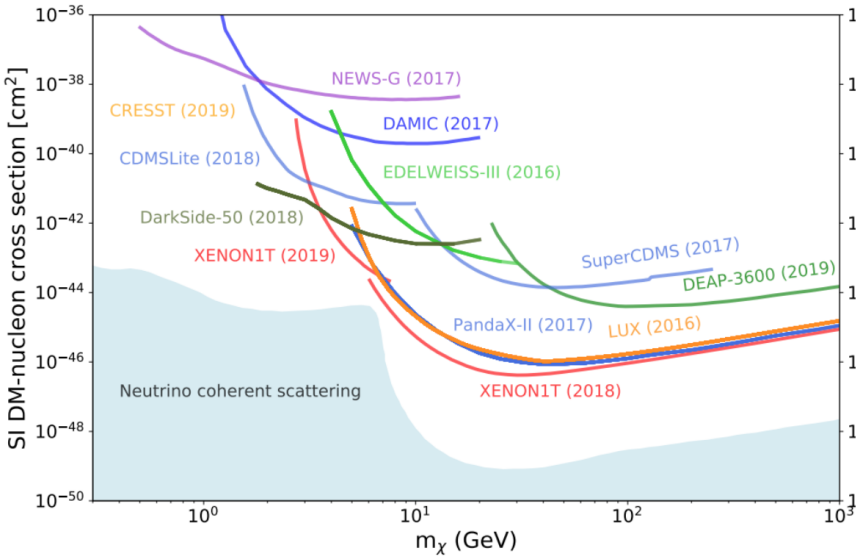

Figure 1.3: Spin-independent (SI) cross section as a function of dark matter mass, for a collection of different experiments. The curves indicate a lower bound on the scattering cross section.

Throughout the remainder of this paper we will only be concerned with indirect detection methods, though we will make use of the results shown in Figure 1.3.

1.3 Light Dark Matter Through Quark Currents

Recently, there has been significant interest in models of dark matter (DM) in which the dark matter particle has a mass $m_\chi \lesssim \mathcal{O}(\text{GeV})$. This is appealing because such models evade nearly all constraints on DM imposed by direct detection experiments, since direct detection experiments are insensitive to the small recoil energies characteristic of $m_\chi \lesssim \mathcal{O}(\text{GeV})$. If this sub-GeV dark matter annihilates or decays into SM particles, then the energies of these final-state particles are produced with energies in the $\mathcal{O}(\text{MeV})$ range. In the case that these final state particles decay into photons, such a process would in principle be astrophysically observable. In this case, one could then detect the indirect signatures of dark matter by probing dark matter dominated regions of space and searching for an excess of these photons. In Chapters 2 and 3, we will derive this photon signal directly from our models and determine bounds imposed on the model's parameters by current diffuse background emission observations and future observations of dwarf spheroidal galaxies (dSphs).

Dwarf spheroidal galaxies are currently believed to be among the most dark matter dominated regions in the universe [43], with mass-to-light ratios of the order $\mathcal{O}(10^2 M_\odot)$ [44–47]. As such, dSphs provide a unique and fertile testing field for searches of indirect signals predicted by theories of dark matter which couple to the standard model. In Chapters 2 and 3 we will derive constraints imposed on our dark matter model by future indirect DM searches of dSphs. Specifically, we will consider these constraints as they apply to a future indirect search of the Draco galaxy.

For the reasons above, there has been recent interest in sub-GeV dark matter which specifically couples to quarks [4–10]. This is because at low energies, all of the ingredients for indirect detection are present: the DM will directly couple to neutral pions (and other mesons; instead of free quarks) through contact interactions, and these mesons will then decay to photons leaving behind a characteristic photon spectrum.

In Chapters 2 and 3 we consider models wherein dark matter interacts with a current composed of quarks q interacts with a spin-1 field Z^μ with coupling strength α_q. The most general expression of a quark current Q^μ is an operator of the form

$$Q^\mu = \overline{q}\Gamma^\mu q, \tag{1.4}$$

where Γ^μ is a Dirac bilinear. Then the interaction Lagrangian for a general quark current coupling to Z^μ with strength α_q is given by

$$\mathcal{L}_{int} = \sum_{q \text{ quarks}} \alpha_q Z_\mu (\overline{q}\Gamma^\mu q). \tag{1.5}$$

Now, in Chapter 2 we will consider two models. The first model will be a model of dark matter decay where we take Z^μ to be a single spin-1 dark matter particle X^μ. This particle will couple to a vector quark current and so will be able to decay to Standard Model particles. For a vector current interaction, the Dirac matrix is simply $\Gamma^\mu = \gamma^\mu$. So for this model, the interaction Lagrangian is given by

$$\mathcal{L}_{int} \;=\; g \sum_q \alpha_q X_\mu (\overline{q}\gamma^\mu q), \tag{1.6}$$

where g is an overall scaling constant.

The second model we consider in Chapter 2 is a model of dark matter annihilation wherein we take dark matter to be a Dirac fermion χ. We take Z^μ to be an effective spin-1 non-renomalizable operator $\overline{\chi}\gamma^\mu\chi/\Lambda^2$, where Λ is the energy scale of new physics. So for this case the interaction with the quark current is given by

$$\mathcal{L}_{int} = \sum_q \frac{\alpha_q}{\Lambda^2}(\bar{\chi}\gamma^\mu\chi)(\bar{q}\gamma_\mu q). \tag{1.7}$$

In Chapter 3 we again take dark matter to be a Dirac fermion χ, and concern ourselves only with dark matter annihilation. However, instead of a vector current Dirac bilinear of the fermions we rather consider an axial-vector current interaction. For an axial-vector current interaction, the Dirac matrix is given by $\Gamma^\mu = \gamma^\mu\gamma^5$. So in this model the dark matter interaction with the quark current is given by

$$\mathcal{L}_{int} = \sum_q \frac{\alpha_q}{\Lambda^2}(\bar{\chi}\gamma^\mu\gamma^5\chi)(\bar{q}\gamma_\mu\gamma^5 q). \tag{1.8}$$

In Chapters 2 and 3 we will fully explore the implications of these dark matter models, calculating their photonic signatures and analyzing it in the context of current and future observations.

1.4 Dark Matter Freeze Out during an Early Cosmological Period of QCD Confinement

There are a plethora of theoretical ideas and models as to how to incorporate dark matter, and exploring how to test them is a major area of activity in particle experiment. Among the various dark matter candidates, the class of weakly interacting massive particles (WIMPs) remains extremely attractive, largely driven by the appealing opportunity to explain their relic density based on the strength of their interactions with the SM.

Conventional theories of WIMPs are challenged by the null results from direct searches for dark matter scattering with heavy nuclei [50]. For many generic models of WIMP interactions with the SM, these searches exclude the required annihilation cross section for masses 1 GeV $\lesssim m_\chi \lesssim 10^4$ GeV. While it is possible to contrive interactions which the requisite cross section that suppress scattering (see [57–63] for a few examples), these restrictions along with the null results of WIMP searches [52–55], suggest that either Nature has been unkind in choosing which model of WIMPs to realize, or there is tension between realizing the observed relic density and the limits from experimental searches for WIMPs

However, a key assumption under-pinning the mapping of the relic density to WIMP searches today is that the cosmological history of the Universe can be reliably extrapolated back to the time of freeze out. The standard picture extrapolates based on a theory containing the SM plus dark matter (and dark energy), with no other significant ingredients. The success of Big Bang Nucleosynthesis (BBN) in explaining the primordial abundances of the light elements could be taken as an argument that it is unlikely that cosmology has been very significantly altered at temperatures lower than $\sim$ 10 MeV, but this is far below the typical freeze-out temperature of a weak scale mass WIMP, which is more typically in the 5-100 GeV range. Indeed, it has been shown that an early period of matter domination [65] or late entropy production [64] can alter the relic abundance for fixed WIMP model parameters, leading

to substantially different mapping between the observed abundance and the expectations of direct searches.

In Chapter 4, we explore a nonstandard cosmology in which QCD undergoes an early phase of confinement. If dark matter freeze out occurs during this early confinement, then the dark matter-meson interactions are scaled up in proportion to the increased confinement scale. This scaled up interaction leads to a strikingly different annihilation cross section at the time of freeze-out than during the period which current observations have bearing. We will find that depending on the underlying form of the dark matter interactions with quarks, radical departures from the expected relic density are possible.

Chapter 2

Dark Matter Coupling to Quarks: The Vector Portal

This chapter heavily relies on previously published work in collaboration with Arvind Rajaraman and Jason Kumar [42].

2.1 Introduction

Recently, there has been significant interest in models of dark matter (DM) in which the dark matter particle has a mass $m_X \lesssim \mathcal{O}(\text{GeV})$. These models can evade the tight constraints on dark matter placed by direct detection experiments, since these experiments typically lose sensitivity at low mass. If dark matter with $m_X \lesssim \mathcal{O}(\text{GeV})$ annihilates or decays in the cosmos, the photons produced will tend to lie in the current "MeV-gap" in observational sensitivity, but a variety of new instruments (such as e-ASTROGAM [1], AMEGO [2] and APT [3]) are being developed to fill this gap. Such instruments would be well-positioned for indirect detection searches for MeV-range dark matter.

There has been particular recent interest in MeV-range dark matter which couples largely to light quarks [4–10]. The reason is because the hadronic final states which can be produced at such small center-of-mass energies are largely constrained by kinematics and symmetry. Moreover, several of the accessible hadrons, such as π^0 and η, produce striking photon signals when they decay. This scenario is thus particularly appealing from the point of view of indirect detection.

Recent work has considered the case where dark matter couples to either scalar, pseudoscalar, or axial-vector quark bilinears [10]. But if the dark matter couples to a quark vector current, then the leading accessible final state (at low center-of-mass energy) is $\pi^+\pi^-$, whose decays produce few photons, making this case difficult to probe. In this work, we extend this analysis to higher energies, where new final states are allowed . We determine the photon spectrum which will be produced for a variety of choices of the flavor structure of DM-Standard Model (SM) interactions, and determine the sensitivity of proposed experiments.

We will be interested in the case where dark matter appears as a vector spurion. We assume that electroweak couplings are only relevant for the decays of hadrons produced by dark matter annihilation/decay. As described in [10] (see also [11]), DM-SM interactions can then be understood using chiral perturbation theory, where dark matter is introduced as a spurion which breaks Standard Model flavor symmetries. The chiral Lagrangian used for the analysis in [10] only involved the pseudoscalar meson octet. But since this work will consider a higher mass range, we must also introduce the vector meson octet, following the approach of [18]. We will find that the dominant photon signal arises from the production of π^0, either directly or from the decays of K_L, K_S, $K^\pm$, ρ or ω.

The plan of this paper is as follows. In Section II, we will describe the application of chiral perturbation theory to the interaction of low-mass dark matter with quark vector currents. In Section III, we will describe the generation of the photon spectrum through primary and secondary decays of the hadronic final state particles. In Section IV, we will present

the sensitivities which can be expected from proposed experiments. We conclude with a discussion of our results.

2.2 The Application of Chiral Perturbation Theory to Dark Matter Interactions With Vector Currents

We will consider two models in which dark matter either decays or annihilates through a coupling to a vector quark current. In the first model of dark matter decay, a single spin-1 dark matter particle (X_μ) couples to the vector quark current and can decay to Standard Model particles. For this model,

$$\mathcal{L}_{int} = g \sum_q \alpha_q X^\mu \bar{q} \gamma_\mu q, \tag{2.1}$$

In the second model, we take dark matter to be a Dirac fermion (χ) which couples to quarks through a vector-vector interaction. In this model we take

$$\mathcal{L}_{int} = \sum_q \frac{\alpha_q}{\Lambda^2} \bar{\chi} \gamma^\mu \chi \bar{q} \gamma_\mu q, \tag{2.2}$$

For the application to chiral perturbation theory, it is useful to consider these interactions as couplings of the quark vector current to a spurion v_q^μ where,

$$v_q^\mu = g \alpha_q X^\mu, \text{ or } \frac{\alpha_q}{\Lambda^2} \bar{\chi} \gamma^\mu \chi. \tag{2.3}$$

Note that this interaction generically breaks the $SU(3)_L \times SU(3)_R$ flavor symmetries of low-energy QCD.

We note that there is a specific case, viz. $\alpha_u = -2\alpha_d = -2\alpha_s$, which corresponds to the electromagnetic coupling. For this particular coupling, the dark matter annihilation rates can be obtained by using data from e^+e^- to hadrons. However, for a more general relation between the couplings, we cannot use this data, and the chiral Lagrangian is essential.

We will take the mass of the dark matter to be in the GeV range; we shall be more specific shortly. In this range the decay/annihilation products cannot be treated as weakly coupled propagating quarks. We assume that the dominant final states produced by low-mass dark matter interactions with quarks are hadronic, and that primary interactions which scale as α_{EM} or sG_F are negligible. Since the coupling of dark matter to light hadrons is governed by QCD and the dark matter-quark current contact interaction, we can directly express the coupling of dark matter to light mesons using a chiral Lagrangian in which dark matter appears as a spurion which breaks Standard Model flavor symmetries.

This approach was followed in [10], under the assumption that $\sqrt{s} \lesssim 2m_{K^\pm}$. In this case, the only accessible hadrons are π^0, $\pi^\pm$ and η, and one can describe DM-SM interactions using a chiral Lagrangian involving only the spurions and the pseudoscalar meson octet. But in the case in which dark matter only interacted with quark vector currents, it was found that the only accessible two-body final state was $\pi^+\pi^-$. Since the decays of charged pions produce very few photons, this channel is not useful for the purpose of indirect detection with gamma-ray telescopes.

We now redo this analysis for dark matter masses where vector mesons are kinematically accessible. We will focus on the energy range 0.91 GeV $\leq E_{cm} \leq$ 1.15 GeV. Below this energy range, the only two-body final state which is allowed by symmetry and kinematics is $\pi^+\pi^-$, and this state produces few photons, leading to reduced sensitivity for gamma-ray

experiments. We also do not consider larger energies, in order to avoid final states involving glueballs.

The allowed final states from a dark matter initial state are restricted by symmetry considerations. The only kinematically accessible neutral two-body final states with vanishing net strangeness are $\pi\pi$, $\eta\eta$, $\eta\pi^0$, $\rho\pi$, $\omega\pi^0$, K^+K^-, $K^0\bar{K}^0$. If dark matter couples to a vector quark current, the final state necessarily has $J^{PC} = 1^{--}$. As such, the $\pi^0\pi^0$, $\eta\pi^0$, $\eta\eta$, K_LK_L and K_SK_S final states are forbidden. As a result, the only final states which we need consider are $\pi^+\pi^-$, K^+K^-, K^LK^S, $\rho\pi$, and $\omega\pi^0$. We will use the chiral lagrangian to see that indeed all these final states can be accessed.

We write the chiral Lagrangian for the pseudoscalar meson octet to lowest order in the p^2 expansion. As the flavor symmetries of low-energy QCD are broken by the insertion of the v_q^μ in the fundamental Lagrangian through eq. 2.1, the v_q^μ must also appear in the chiral Lagrangian as spurions which break the flavor symmetries. The form of these interactions is determined at this order by symmetry considerations, and chiral Lagrangian can be expressed (see [13–17]) as

$$\mathcal{L}_\Phi = \frac{F^2}{4} Tr\left[(\partial_\mu U - iv_\mu U + iUv_\mu)\left(\partial^\mu U^\dagger + iU^\dagger v_\mu - iv_\mu U^\dagger\right)\right], \tag{2.4}$$

where

$$
\begin{aligned}
U &\equiv \exp[\imath\sqrt{2}\Phi/F], \\
\Phi &\equiv \begin{pmatrix} \frac{\pi^0}{\sqrt{2}} + \frac{\eta_8}{\sqrt{6}} & \pi^+ & K^+ \\ \pi^- & -\frac{\pi^0}{\sqrt{2}} + \frac{\eta_8}{\sqrt{6}} & K^0 \\ K^- & \bar{K}^0 & -\frac{2\eta_8}{\sqrt{6}} \end{pmatrix}, \\
v^\mu &\equiv \begin{pmatrix} v_u^\mu & 0 & 0 \\ 0 & v_d^\mu & 0 \\ 0 & 0 & v_s^\mu \end{pmatrix}.
\end{aligned} \tag{2.5}
$$

The pion decay constant is $F \sim 92$ MeV. To a good approximation, η_8 can be equated with the physical η meson, and we do so henceforth.

For two-body final states, the only relevant terms in eq. 3.16 are the following contact interactions

$$
\mathcal{L}_{\text{contact}} = \imath\Big\{(v_d^\mu - v_s^\mu)\bar{K}^0\partial_\mu K^0 + (v_s^\mu - v_u^\mu)K^+\partial_\mu K^- + (v_d^\mu - v_u^\mu)\pi^+\partial_\mu\pi^- - h.c\Big\}. \tag{2.6}
$$

These can produce the two body final states K^+K^-, K^L, K^s and $\pi^+\pi^-$.

Other possible two-body final states involving vector mesons may also be produced. In order to consider these final states, it is necessary to include vector mesons in the chiral Lagrangian. For this purpose, we use the results of [18]. We found that no new two-body final states can be produced directly by a contact interaction involving the vector meson octet, but they can be produced through a coupling of dark matter to an intermediate vector meson. We thus need the couplings of a vector meson to a vector spurion, and the trilinear couplings

involving at least one vector meson. The relevant part of the chiral Lagrangian was found in [18, 19], and can be written as

$$\begin{aligned}\mathcal{L}_{\Phi_{\mu\nu}} &= -\frac{1}{4}Tr\left[(D^{\mu}\Phi_{\mu\alpha})(D_{\nu}\Phi^{\nu\alpha})\right]+\frac{1}{8}m_V^2 Tr\left[\Phi^{\mu\nu}\Phi_{\mu\nu}\right]+\frac{1}{2}f_V Tr\left[\Phi^{\mu\nu}f^{+}_{\mu\nu}\right]+\frac{i}{2}f_V h_P \mathrm{tr}\left(U_{\mu}\Phi^{\mu\nu}U_{\nu}\right)\\ &+\frac{i}{8}h_A\varepsilon^{\mu\nu\alpha\beta}\mathrm{tr}\left(\{\Phi_{\mu\nu},(D^{\tau}\Phi_{\tau\alpha})\}U_{\beta}\right)+\frac{i}{8}h_O\varepsilon^{\mu\nu\alpha\beta}\mathrm{tr}\left([D_{\alpha}\Phi_{\mu\nu},\Phi_{\tau\beta}]U^{\tau}\right), \qquad (2.7)\end{aligned}$$

where

$$\begin{aligned}\Phi_{\mu\nu} &= \sqrt{2}\begin{pmatrix}\frac{\rho_{\mu\nu}}{\sqrt{2}}+\frac{\omega_{\mu\nu}}{\sqrt{2}} & \rho^{+}_{\mu\nu} & K^{*+}_{\mu\nu}\\ \rho^{-}_{\mu\nu} & -\frac{\rho_{\mu\nu}}{\sqrt{2}}+\frac{\omega_{\mu\nu}}{\sqrt{2}} & K^{*0}_{\mu\nu}\\ K^{*-}_{\mu\nu} & \bar{K}^{*0}_{\mu\nu} & \phi_{\mu\nu}\end{pmatrix},\\ f^{+}_{\mu\nu} &= \frac{1}{2}\left[e^{\imath\Phi/\sqrt{2}F}\left(\partial_{\mu}v_{\nu}-\partial_{\nu}v_{\mu}\right)e^{-\imath\Phi/\sqrt{2}F}+e^{-\imath\Phi/\sqrt{2}F}\left(\partial_{\mu}v_{\nu}-\partial_{\nu}v_{\mu}\right)e^{\imath\Phi/\sqrt{2}F}\right],\\ U_{\mu} &= \frac{1}{2}e^{-\imath\Phi/\sqrt{2}F}\left(\partial_{\mu}e^{\imath\sqrt{2}\Phi/F}\right)e^{-\imath\Phi/\sqrt{2}F}-\frac{\imath}{2}e^{-\imath\Phi/\sqrt{2}F}v_{\mu}e^{\imath\Phi/\sqrt{2}F}+\frac{\imath}{2}e^{\imath\Phi/\sqrt{2}F}v_{\mu}e^{-\imath\Phi/\sqrt{2}F},\\ D_{\alpha}\Phi_{\mu\nu} &= \partial_{\alpha}\Phi_{\mu\nu}+[\Gamma_{\alpha},\Phi_{\mu\nu}],\\ \Gamma_{\alpha} &= \frac{1}{2}e^{-\imath\Phi/\sqrt{2}F}\left(\partial_{\mu}-\imath v_{\mu}\right)e^{\imath\Phi/\sqrt{2}F}+\frac{1}{2}e^{\imath\Phi/\sqrt{2}F}\left(\partial_{\mu}-\imath v_{\mu}\right)e^{-\imath\Phi/\sqrt{2}F},\end{aligned}$$

The cubic couplings between vector and pseudoscalar meson octets are

$$\begin{aligned}\mathcal{L}_{\mathrm{int}} \supset & -\frac{\sqrt{2}h_A}{F}\varepsilon^{\mu\nu\alpha\beta}\left[\frac{1}{2}\partial_{\beta}\pi^0\left(\rho^0_{\mu\nu}\partial^{\tau}\omega_{\tau\alpha}+\omega_{\mu\nu}\partial^{\tau}\rho^0_{\tau\alpha}\right)+\partial_{\beta}\pi^{-}\left(\rho^{+}_{\mu\nu}\partial^{\tau}\omega_{\tau\alpha}+\omega_{\mu\nu}\partial^{\tau}\rho^{+}_{\tau\alpha}\right)+c.c\right]\\ &-\frac{h_O}{\sqrt{2}F}\varepsilon^{\mu\nu\alpha\beta}\left[(\partial_{\alpha}\rho^0{}_{\mu\nu})\left((\partial^{\tau}\pi^0)\omega_{\tau\beta}\right)+\rho^0{}_{\tau\beta}\left((\partial^{\tau}\pi^0)\partial_{\alpha}\omega_{\mu\nu}\right)+\left(\partial^{\tau}\pi^{-}\left(\omega_{\tau\beta}\partial_{\alpha}\rho^{+}{}_{\mu\nu}+\rho^{+}{}_{\tau\beta}\partial_{\alpha}\omega_{\mu\nu}\right)+c.c\right)\right]\\ &+i\frac{8f_V h_P}{F^2}\left[2\partial_{\mu}\pi^{+}\partial_{\nu}\pi^{-}\rho^0{}_{\mu\nu}+\partial_{\mu}\bar{K}^0\partial_{\nu}K^0\left(\rho^0{}_{\mu\nu}-\omega_{\mu\nu}-\sqrt{2}\varphi_{\mu\nu}\right)-\partial_{\mu}K^{-}\partial_{\nu}K^{+}\left(\rho^0{}_{\mu\nu}+\omega_{\mu\nu}-\sqrt{2}\varphi_{\mu\nu}\right)\right] \qquad (2.8)\end{aligned}$$

where m_V, f_V, h_A, h_O and h_P are parameters (the values of the relevant parameters are given in Section 2.5.1).

From these interactions, we find two new possible final states: $\rho\pi^0$ and $\omega\pi^0$.

2.3 Photon Spectra

These primary mesons can then decay through multiple decay modes to produce photons. These can be multistep decay processes; for example, the kaon can decay to pions which subsequently decay to photons. In our case, the primary mesons are $\pi^0, \pi^\pm, K^0, \bar{K}^0, K^\pm, \rho, \omega$, and we need to find the photon spectra produced in their decays. The π^0 decays to two photons essentially 100% of the time, and the $\pi^\pm$ essentially never produce photons. The ρ^0 decays primarily to charged pions, and hence does not produce photons. But decays of $\rho^\pm$ typically produce π^0 as well as $\pi^\pm$, with the subsequent the decays of π^0 yielding photons. For the kaons and the omega, we use the decay modes found in the Particle Data Book [20]. We have tabulated in Table 2.1 the important decay modes of the mesons which we have considered, along with their branching ratios. Decay modes which are not expected to produce a significant number of photons (e.g. decays involving only charged pions) are not shown.

K^+	$\pi^0 e^+ \nu$	5%
	$\pi^0 \mu^+ \nu$	3.4%
	$\pi^+ \pi^0$	20.7%
	$\pi^+ \pi^0 \pi^0$	1.7%
$\rho^\pm$	$\pi^\pm \pi^0$	100%

K^S	$\pi^0 \pi^0$	30.7%
K^L	$\pi^0 \pi^0 \pi^0$	19.5%
	$\pi^+ \pi^- \pi^0$	12.5%
ω	$\pi^+ \pi^- \pi^0$	89%
	$\pi^0 \gamma$	8%

Table 2.1: The relevant decay modes and branching fractions for the mesons produced from dark matter annihilation/decay through the quark vector current portal.

For the two-body decays, the decay spectrum at rest is fixed by kinematics. The three-body decays are described by a Dalitz plot, which parametrizes the decay kinematics in terms

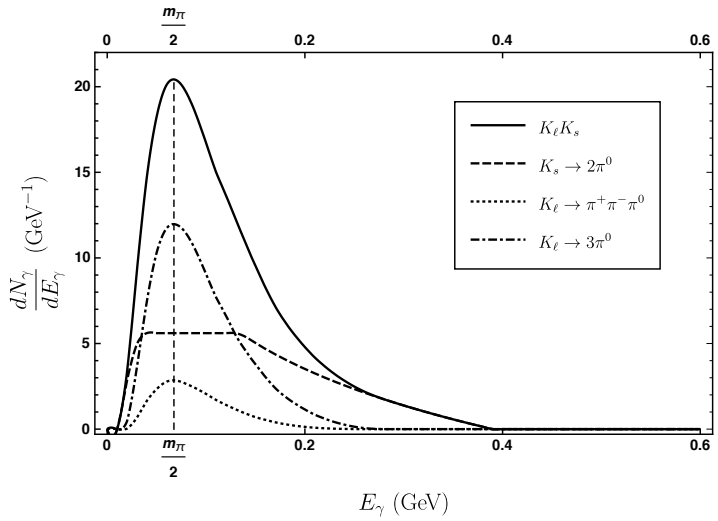

Figure 2.1: Photon spectrum from neutral kaon production ($K_L K_S$). The center-of-mass energy has been taken to be 1.14 GeV.

of the final state energies. We use these to find the decay spectrum at rest for each decay mode of each meson. These details are presented in Appendix A.3. Finally, these mesons are produced and decay with large boosts which also modify the spectrum. The boosting procedure is general, and is described in Appendix A.4.

For illustrative purposes, we show in Figure 2.1 the photon spectrum obtained through the production of neutral kaons produced from dark matter annihilation or decay, assuming the $E_{cm} = 1.14$ GeV. The individual spectra have been weighted according to the branching fractions. It is interesting to compare this spectrum to those found in [10], for the case where dark matter coupled to scalar, pseudoscalar or axial-vector quark currents. In those cases, even though the center-of-mass energy was taken to be ≤ 1 GeV, the typical photon energy was nearly 4 times larger than found here. The reason is because in the case of a scalar, pseudoscalar or axial-vector spurion, one can produce an η in the final state, whose decays yield photons. In the case of a vector spurion, however, almost all photons arise from π^0 decay. As is discussed in Appendix A.4, the photons produced by π^0 decay yield a signal with a peak at $m_\pi/2$, as can be seen in the plot above, resulting in a typical photon energy which is considerably smaller than that of the photons produced from η decay.

2.4 Comparisons to Observations

Following [10], we consider constraints on the obtained photon spectrum from observations of diffuse photon emission, and from future observations of photon emission from a dwarf galaxy (Draco). We will take as a benchmark, an experiment with a fractional 1σ energy resolution of $\epsilon = 0.3$ and an exposure of $I_{exp} = 3000$ cm^2 yr. Since our predicted signal peak is at $m_\pi/2$, we will consider a bin of photon energies centered at $E_0 = m_\pi/2$. and a width of $0.3E_0$ i.e. a bin between $E_- = (m_\pi/2)(1-\epsilon)$ and $E_+ = (m_\pi/2)(1+\epsilon)$. We account for instrumental energy resolution by convolving the injected photon spectrum with a Gaussian smearing function

$$R_\epsilon(E_{obs.}, E_\gamma) \;=\; \frac{1}{\sqrt{2\pi}\epsilon E_\gamma} \exp\left(-\frac{(E_{obs.} - E_\gamma)^2}{2\epsilon^2 E_\gamma^2}\right). \tag{2.9}$$

For each channel p, we determine how many photons are produced per annihilation/decay within the energy bin $E_- \leq E \leq E_+$. These are listed as N_p in Table 2.2.

Channel	N_p
K^+K^-	0.2471
K_LK_S	0.7599
$\rho^0\pi^0$	0.31473
$\omega^0\pi^0$	0.72438
$\rho^\pm\pi^\mp$	0.24213

Table 2.2: Average number of photons produced within the energy window from a single DM decay/annihilation process, given that the particles in the left-most columns are produced.

For the annihilation process, we define an effective cross section $\langle\sigma_A v\rangle_{eff}$ by weighting the theoretical cross sections for each channel p with the acceptance factor N_p, and similarly we

define an effective decay lifetime Γ_{eff}; explicitly

$$\begin{aligned} \langle \sigma v \rangle_{eff} &= \sum_{\text{channels}} \langle \sigma v \rangle_p N_p = \langle \sigma v \rangle_{total} \langle N_p \rangle \\ \Gamma_{eff} &= \sum_{\text{channels}} \Gamma_p N_p = \Gamma_{total} \langle N_p \rangle, \end{aligned} \tag{2.10}$$

where

$$\langle N_p \rangle \equiv \sum_{\text{channels}} Br_p N_p, \tag{2.11}$$

and where $\langle \sigma v \rangle_{total}$ is the total annihilation cross section, Γ_{total} is the total decay width, and Br_p is the branching fraction to channel p.

Given the branching fractions to all final states, one can compute $\langle N_p \rangle$, and a bound obtained from data on $\langle \sigma v \rangle_{eff}$ or Γ_{eff} can be directly translated into a bound on the total annihilation cross section or decay width.

Note that, for all of the channels given in Table 2.2, the highest and lowest N_p differ by at most a factor of 3. Although the branching fractions could be computed using the chiral Lagrangian, one could worry about higher order corrections. However, as long as dark matter annihilation/decay proceeds almost entirely to the final states that we consider (i.e. if $\sum_{\text{channels}} Br_p \sim 1$), then $\langle N_p \rangle$ can be corrected by at most a factor of ~ 3, as that is the largest ratio of acceptance factors between any channels. Thus, these corrections could only change bounds on the total annihilation cross section or decay rate by a factor of at most ~ 3. The only exception is the $\pi^+\pi^-$ final state, for which $N_p \sim 0$; if this final state is allowed by the symmetries of the theory, then the relationship between the effective annihilation cross section (decay width) and the total annihilation cross section (decay width) is more

dependent on the branching fractions. But this final state is not allowed if $\alpha_u = \alpha_d$, as a result of isospin symmetry. Moreover, the branching fraction to $\pi^+\pi^-$ is related to the branching fraction to K^+K^- and K_LK_S by flavor symmetry, as seen from eq. 2.6. As such, the ratio of these branching fractions cannot receive large corrections.

The total photon signal N_S is

$$N_S = \frac{\Xi_{eff}^{ann.,dec.}}{4\pi m_X} \overline{J}^{ann.,dec.} (I_{exp}\Delta\Omega) \tag{2.12}$$

where

$$\Xi^{ann.} = \frac{\langle \sigma_A v \rangle_{eff}}{2m_X} \qquad \Xi^{dec.} = \Gamma_{eff}, \tag{2.13}$$

and $\bar{J}^{ann.,dec.}$ are the average J-factors of the target for either dark matter annihilation or dark matter decay. For diffuse emission, the average J-factors are [27]

$$\begin{aligned} \bar{J}_{dif.}^{ann.} &= 3.5 \times 10^{21}\ \text{GeV}^2\ \text{cm}^{-5}\text{sr}^{-1}, \\ \bar{J}_{dif.}^{dec.} &= 1.5 \times 10^{22}\ \text{GeV}\ \text{cm}^{-2}\text{sr}^{-1}, \end{aligned} \tag{2.14}$$

while for Draco, the average J-factors are [28]

$$\begin{aligned} \bar{J}_{Draco}^{ann.} &= 6.94 \times 10^{21}\ \text{GeV}^2\ \text{cm}^{-5}\ \text{sr}^{-1}, \\ \bar{J}_{Draco}^{dec.} &= 5.77 \times 10^{21}\ \text{GeV}\ \text{cm}^{-2}\ \text{sr}^{-1}. \end{aligned} \tag{2.15}$$

2.5 Results

For diffuse emission, we restrict attention to latitudes greater than $> 20^{\circ}$. In this region, and in the energy range 0.8 MeV - 1 GeV, the isotropic flux observed by COMPTEL and EGRET can be well fit [4, 21] to the function

$$\frac{d^2\Phi^{iso.}}{d\Omega\ dE_{obs.}} = 2.74 \times 10^{-3} \left(\frac{E_{obs.}}{\mathrm{MeV}}\right)^{-2.0} \mathrm{cm}^{-2}\mathrm{s}^{-1}\mathrm{sr}^{-1}\mathrm{MeV}^{-1}. \tag{2.16}$$

The expected number of observed events between the energies E_- and E_+ is then given by

$$N_O = 8.6 \times 10^4 \left(\frac{\mathrm{MeV}}{E_-} - \frac{\mathrm{MeV}}{E_+}\right) \frac{(I_{exp.}\Delta\Omega)}{\mathrm{cm}^2\ \mathrm{yr\ sr}}. \tag{2.17}$$

We impose the condition that within any such energy bin, the number of expected signal events should not exceed the number of expected observed events i.e., we require $N_S < N_O$. This constitutes a conservative bound; since we assume no knowledge of the background photon spectrum, we conservatively assume that the background could be negligible in any energy bin.

For a dwarf spheroidal galaxy, such as Draco, the background consists of all photons emitted by astrophysical processes as well as dark matter annihilation/decay along the line of sight to the dwarf, but not within the dwarf. This background can be estimated purely from data by considering the observed flux in the direction of the dSph, but slightly off-axis [22–26]). Although one would follow this approach in an actual analysis of data from a future instrument, for our purposes, we can estimate the background flux to be roughly the same as observed diffuse flux given in eq. 3.19. If we assume that the number of observed events

is the same as the expected number of background events, then a model can be ruled out at $n-\sigma$ confidence level if $N_S > n\sqrt{N_O}$. We also assume that the experimental angular resolution is smaller than the size of Draco (1.3°).

The constraint on dark matter annihilation from the diffuse emission is

$$\langle \sigma_A v \rangle_{eff} \sim 6.22 \times 10^{-26} \text{ cm}^3 \text{ s}^{-1} \tag{2.18}$$

while the constraint on the lifetime is

$$\Gamma_{eff} \sim 2.55 \times 10^{-26} \text{ s}^{-1} \tag{2.19}$$

A similar study of dark matter annihilation/decay in Draco could yield a 2σ constraint on dark matter annihilation of

$$\langle \sigma_A v \rangle_{eff} \lesssim 9.83 \times 10^{-28} \text{ cm}^3 \text{ s}^{-1} \tag{2.20}$$

while the constraint on the lifetime would be

$$\Gamma_{eff} \lesssim 2.07 \times 10^{-27} \text{ s}^{-1} \tag{2.21}$$

The Planck bound on the rate of electromagnetic decays is $\Gamma_{total} \sim \mathcal{O}(10^{-24})$ s^{-1} [4, 29, 30].

Our sensitivity is to the effective decay width, which differs from Γ_{total} by a factor $\langle N_p \rangle$ (which depends on the flavor structure of the quark couplings). But this factor is always $\mathcal{O}(1)$ for any choice of flavor structure, so the sensitivity obtainable from indirect detection is typically at least an order of magnitude better than the Planck bound.

We can also convert these to bounds on the fundamental couplings. This calculation is contaminated by uncertainties in the chiral Lagrangian at high energies. Nevertheless, we now present estimates for such bounds in the following subsection (2.5.1).

2.5.1 Tree Level Bounds on Parameters

Here we calculate the bounds on the fundamental scale corresponding to the bounds on the effective cross-section and lifetime found earlier. We work to tree level in the chiral Lagrangian; higher order effects may produce deviations from these results, but we believe that our estimates should be accurate to a factor of a few.

We calculate the cross section using the Lagrangians (3.16, 2.7, 2.8). The various parameters are [18, 19]

$$\begin{aligned} f_V &= (140 \pm 14) \text{ MeV}, \\ m_V &\sim 0.764 \text{ GeV}, \\ h_A &= 2.33 \pm 0.03, \\ h_P &\sim 1.75 \end{aligned} \tag{2.22}$$

We consider two classes of models. In the first class we assume isospin is a good symmetry, and we set $\alpha_u = \alpha_d$. In the second class we set $\alpha_s = 0$.

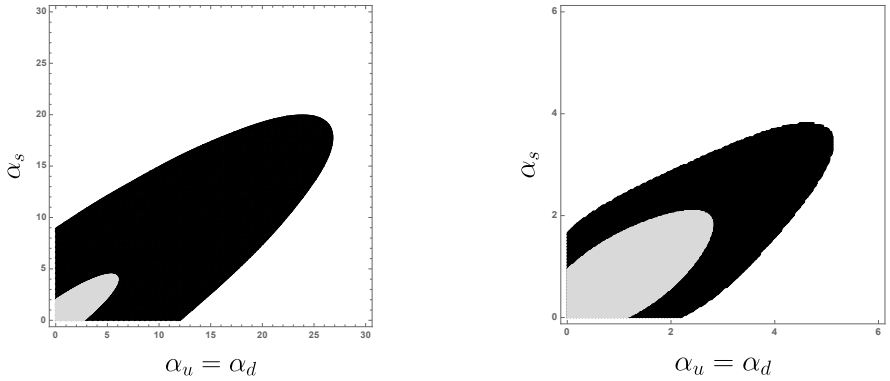

Figure 2.2: Bounds on the parameter space from annihilation (left panel, $\Lambda = 100$ GeV) and decay (right panel, $g = 10^{-24}$) on theories with $\alpha_u = \alpha_d$, assuming $E_{cm} = 1.14$ GeV. The region in black is allowed by constraints on diffuse emission, while the grey region demarcates the sensitivity of a search for emission from Draco.

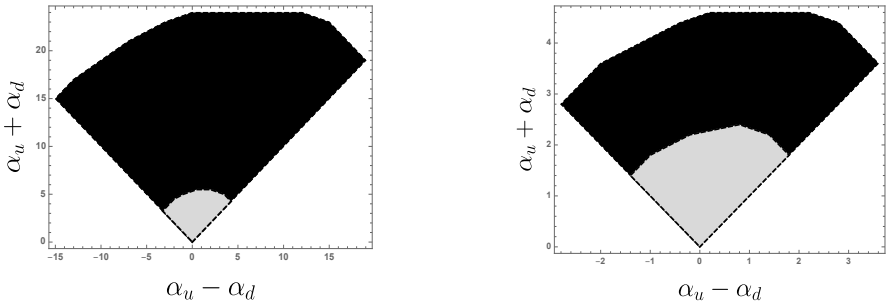

Figure 2.3: Bounds on the parameter space from annihilation (left panel, $\Lambda = 100$ GeV) and decay (right panel, $g = 10^{-24}$) on theories with $\alpha_s = 0$, assuming $E_{cm} = 1.14$ GeV. The region in black is allowed by constraints on diffuse emission, while the grey region demarcates the sensitivity of a search for emission from Draco.

Bounds on the parameter space of the first class of models are shown in Figure 2.2. Bounds on the parameter space of the second class of models are shown in Figure 2.3. In each case, we have normalized the couplings to have $g = 10^{-24}$ in equation (2.1), and $\Lambda = 100$ GeV in equation (3.1). In all cases we have set the center-of-mass energy to be $E_{cm} = 1.14$ GeV. Because we consider a narrow energy range lying between the $\rho\pi$ threshold (~ 0.91 GeV) and our upper cutoff (1.15 GeV), these constraints do not change dramatically as we change the center-of-mass energy. But there is one feature worthy of note; if $E_{cm} \sim 1.02$ GeV and if dark matter couples to a strange quark vector current, then dark matter can annihilate through an intermediate ϕ near resonance. In this case, the constraints on α_s which could

be obtained from indirect detection would improve dramatically. But aside from near this resonance, sensitivity throughout the energy range 0.91 GeV $\leq E_{cm} \leq$ 1.15 GeV is well approximated by results at $E_{cm} = 1.14$ GeV. Note that the ρ^0 and ω resonances lie below the kinematic range we consider.

Note also that, if the dark matter coupling does not break isospin, then the constraints on the couplings are weakest if $\alpha_u = \alpha_d = \alpha_s$. This can easily be understood from equation (2.6); if all light quark couplings are identical, the dark matter coupling to the pseudoscalar meson octet vanishes. In this limit, the only remaining channels which produce photons are $\omega\pi^0$ and $\rho\pi$.

2.6 Conclusions

We have considered dark matter coupled to Standard Model quarks through vector currents of the form $\bar{q}\gamma^\mu q$. We have utilized the chiral Lagrangian to obtain couplings of the dark matter to mesons, and found the photon spectrum from dark matter decay (if the dark matter itself is a vector) or from annihilation (where it is a Dirac fermion). We have found that current observations of the diffuse photon spectrum already can be used to constrain the parameter space of these models. Future observations of dwarf spheroidal galaxies will significantly improve these bounds or may discover these models.

In the case of dark matter decay, these constraints exceed those obtainable from Planck [29] (from the effect of late-time energy injection on the CMB) by about an order of magnitude. We note that the low value of the mass weakens direct detection bounds, and for certain couplings (e.g. couplings only to strange quarks), the bounds are extremely weak. In particular, for $m_\chi \sim 500$ MeV, the upper bound on spin-independent (SI) dark matter-nucleon scattering found by CRESST [31] is $\sigma_{\rm SI} \sim \mathcal{O}(10^{-1})$ pb. For a scenario of dark matter anni-

hilation through coupling to the quark vector portal, DM-nucleon scattering would be spin and velocity-independent. If we set $\alpha_u = \alpha_d \sim 3$, $\alpha_s = 0$ (the limit of sensitivity for a search for emission from Draco), one would find $\sigma_{\rm SI} \sim \mathcal{O}(10)$ pb, about two orders of magnitude above current bounds from CRESST. However, CRESST's sensitivity is greatly reduced for the case of isospin-violating dark matter [32–34] ($\alpha_u = -\alpha_d$, $\alpha_s = 0$), and is essentially unconstraining for the parameter space of interest here. Similarly, if dark matter only couples to the strange quark vector current ($\alpha_u = \alpha_d = 0$), then the SI scattering cross section vanishes, and there are no meaningful constraints from direct detection.

We have found that if dark matter couples to a vector quark current, then the typical photon energy is roughly a factor of 4 smaller than in the scenarios considered in [10], wherein dark matter coupled to scalar, pseudoscalar or axial-vector currents. This result is largely independent of the center-of-mass energy of the process, but is instead dictated by the Lorentz and flavor structure of the dark matter-quark current coupling, which determines whether or not an η can be produced in the final state.

Chapter 3

Dark Matter Coupling to Quarks: The Axial-Vector Portal

3.1 Introduction

In this section, we will consider MeV-range cold dark matter which couples to quarks as an axial-vector current. Previous work has been done on this [10] at CM energies $\sim \mathcal{O}(\text{GeV})$, but considers only the dominant $\pi^0\pi^0\eta$ process (which is inaccessible at the CM energies we consider). Moreover, the analysis therein is carried out at CM energies close to the confinement scale (Λ_{QCD}), and so does not lend itself to a perturbative analysis and provides loose upper bounds on the DM branching ratios and not the model parameters themselves. As noted before, at CM energies near Λ_{QCD} there are many additional kinematically accessible final mesonic final states which decay to photons one has to consider. As a result, the net photon signal becomes dominated by the spectrum produced by the $\pi^0\pi^0\eta$ process, and so while the bounds obtained on the effective cross sections found in [10] are of coarse still true, they become much more stringent for the dark matter masses we consider coupling to quarks

as an axial-vector.

We take dark matter to be cold and have mass $m_\chi \sim 350$ MeV, and so the CM energy of the annihilation process is $\sqrt{s} \sim 2m_\chi \sim 700$ MeV. Further, we make no assumptions about the flavor structure of the DM couplings to the quarks. One of the more salient properties of dark matter coupling as an axial-vector to dark matter is how it differs from other portals, such as the vector-like portal we covered in Chapter 2. As we will see, the meson spectrum characteristic of the axial couplings differs drastically from that of the vector-current coupling, in such a way that it is significantly more conducive to photon production at lower DM masses—making it a prime candidate for indirect detection probes.

The layout of this chapter is as follows. In Section II, we present a brief overview of the model we consider, introducing the coupling of dark matter the quark axial-vector current. In Section 3.3 we argue the meson spectrum that results from our model by considerations of quantum numbers. In Section 3.4 we outline a useful general method of estimating the resultant photon spectrum, using only the knowledge we have of the final states (i.e. without mention to a Lagrangian description). Next, in Section 3.5 we outline and justify the chiral Lagrangian description of the model, the technical details of which can be found in Appendix B.1. Then in Section 3.6 we go over our methods for estimating the photon background and expected experimental signal strength for DM annihilation photon production for current and future observations. Finally, in Section 3.7 we report our findings on the photon signal predicted by our theory and the constraints thereby imposed on the DM branching ratios and the model's parameter space.

3.2 The Model

We consider a model in which dark matter annihilates through a coupling to an axial-vector quark current. In this model, we take dark matter to be a Dirac fermion (χ). The axial-vector coupling to the quarks is given by

$$\mathcal{L}_{int} = \sum_q \frac{\alpha_q}{\Lambda^2}(\bar{\chi}\gamma^\mu\gamma^5\chi)(\bar{q}\gamma_\mu\gamma^5 q). \tag{3.1}$$

It will be useful to denote the axial-vector current which couples to the quarks q with strength coupling α_q as

$$a^\mu = \frac{1}{\Lambda^2}(\bar{\chi}\gamma^\mu\gamma^5\chi), \tag{3.2}$$

where Λ is the expected mass of a new massive particle that would mediate the DM-quark interaction. Note that, in general, this interaction does not respect the $SU(3)_L \times SU(3)_R$ chiral symmetry of massless QCD. However if the α_q couplings do not discriminate between the quarks then this interaction does preserve the approximate low energy $SU(3)_F$ flavor symmetry. As mentioned before, we take the mass of the dark matter to be light at $m_\chi \sim 350$ MeV, which yields a CM energy $\sqrt{s} \sim 700$ MeV well below the confinement scale. Hence we do not expect dark matter to annihilate into freely propagating quarks, but rather into kinematically accessible mesonic final states.

3.3 Meson Spectrum

We now consider the possible mesonic final states of this model. Now, not only do the final states need to be kinematically accessible, they also need to have quantum numbers consistent with the initial state of the dark matter's wavefunction. That is, the final states must have quantum numbers consistent with a spin-1 axial-vector. We can therefore determine the allowed SM final states by imposing the fact that they must have $J^{PC} = 1^{++}$ [35]. Now, recall that both the P-parity and C-parity of a particle are factored into an intrinsic C/P-parity, and an extrinsic C/P-parity which depends on the angular quantum numbers of the wavefunction. Further recall that the overall C/P-parity of a *state* is given by the product of of the intrinsic C/P parities of each particle composing the state times the overall phase contribution from the extrinsic C/P-parity. For a boson, the extrinsic P-parity ($\mathcal{P}$) and extrinsic C-parity ($\mathcal{C}$) of a boson is given by[1]

$$\mathcal{C} : (-1)^{L+S} \qquad \mathcal{P} : (-1)^{L}. \tag{3.3}$$

So, kinematic constraints notwithstanding, the dark matter can decay into any $J = 1$ quark bound state with appropriate P and C. This immediately implies that there can be no single pseudoscalar meson final states, and also no single vector meson final states, since the vector mesons all have $J^P = 1^-$. So if the vector mesons are to appear in final states, they either need to come in pairs or with at least one pseudoscalar meson. However, at the CM energies we consider ($\sqrt{s} \sim 700$ MeV) such vector states are kinematically forbidden, and only become relevant at $\sqrt{s} \gtrsim m_\pi + m_\rho \sim 914$ MeV. It is insightful to compare the final-state spectrum of the axial-vector coupling to dark matter to that of a pure vector coupling, which we now do.

[1] We use $\mathcal{C}, \mathcal{P}$ to denote extrinsic parities of a state and C, P to denote the overall parities of a state.

Final State (1^{--})	E_{tot} (MeV)
$\pi^+\pi^-$	280
K^+K^-	986
K_LK_S	994
$\rho^\pm\pi^\mp$	915

Final State (1^{++})	E_{tot} (MeV)	Order
$\pi^0\pi^+\pi^-$	412	$p+p^3$
$\pi^0\pi^0\pi^0$	405	p^3
$\pi^0(\pi^-)^2(\pi^+)^2$	690	$p+p^3$
$(\pi^0)^3\pi^-\pi^+$	680	$p+p^3$

Table 3.1: (**Right**) All kinematically accessible mesonic final states with quantum numbers consistent with the DM axial-current, and the order in the chiral Lagrangian at which they occur

In order for the final-state quantum numbers to be consistent with the dark matter's initial state, the vector states must be in the $|L,S\rangle = |1,0\rangle$ state and that the axial vector states in the $|L,S\rangle = |1,1\rangle$ state. Each of the vector and axial-vector final states share the same overall phase (-1) due to extrinsic parity. However since the intrinsic parity of pseudoscalar and vector mesons is odd, we must have an odd number of of final state mesons for the axial case, and an even number for the vector case. Considering the kinematic constraints at $\sqrt{s} \sim 700$ MeV, we see that dark matter coupling to the quarks as an axial-vector can only admit final states containing an odd number of pseudoscalar mesons. The vector case is very similar except that the kinematic constraints are far more restrictive insofar as photon production is concerned, and that one is forced into an even number of mesons (as opposed to odd).

In Table 3.1 (left) we have listed the five lightest final states that result from the dark matter coupling to quarks as a vector current, and on the right we have done the same for the axial-vector current. Recalling that $\pi^0 \to 2\gamma$ almost always, and that $\pi^+\pi^-$ nearly never produces photons (i.e. $\lesssim 10^{-5}$ %), it is immediately clear that the axial-vector coupling is far more conducive to photon production for lighter forms of dark matter, since in this case the lightest photon-producing final state happens at $\sqrt{s} \sim 405$ MeV (producing six photons), as opposed to the vector case in which the lightest state is 915 MeV which produces only two photons. Specifically, for the DM mass we consider the vector-current coupling admits zero photon-producing final states and the axial-current coupling admits four of them—all

of these states are shown in Table 3.1 (right).

Lastly, it is important to note that, not only are there four photon-producing final states through the axial-vector portal (as opposed to the zero via the vector portal). What is more is that Table 3.1 (right) is an exhaustive list of *all* of the accessible final states through the axial-vector portal at $\sqrt{s} \sim 700$ MeV. This is because the only accessible final states are combinations of $3, 5, 7 \ldots$ mesons whose net mass is less than 700 MeV. Scanning over all combinations of mesons the reader may verify that those listed in Table 3.1 (right) are the only such final states.

Lastly, we note a convenient consequence of the set of all mesonic final states for the axial-vector case. Namely, since there are no vertices for which the dark matter current couples to an even number of mesons, this means that the tree-level Feynman rules for the DM-meson contact interactions are protected from all 1-loop corrections with mesons running the loop.

In summary, we assume the dark matter is cold, and so we may take the dark matter to be approximately at rest. We take the dark matter to have mass $m_\chi = 350$ MeV so that the CM energy of the DM annihilation process is $\sqrt{s} \sim 2m_\chi \sim 700$ MeV. At this energy only combinations of an odd number (> 1) of the scalar mesons whose mass is less than $\sqrt{s} \sim 700$ MeV are kinematically accessible. In particular, we find that the only final states with the correct quantum numbers which are also kinematically accessible are the $\pi^0\pi^+\pi^-$, $\pi^0\pi^0\pi^0$, $\pi^0\pi^0\pi^0\pi^+\pi^-$ and $\pi^0\pi^+\pi^-\pi^+\pi^-$ states, and that the tree-level Feynman rules for these processes are protected from 1-loop corrections with mesons running the loop.

3.4 Dark Matter Branching Ratios

To obtain coarse estimates of the total DM annihilation cross section in a Lagrangian-free way, we consider constraints placed on the the dark matter branching ratios into the allowed

mesonic final states. We do this by incorporating the observations of diffuse photon emission as well as observations from possible future measurements of the Draco dSph galaxy. In this section we will treat the branching ratios as free parameters and make no mention of the underlying particulars of the model.

Let us first define the effective average cross section $\langle \sigma v \rangle_{eff}$, as the sum over the cross sections through each channel $\langle \sigma v \rangle_c$, weighted by the average number of photons produced by the final state N_c, given that process c occurs. In terms of the branching ratios, the effective cross section is then given by

$$\langle \sigma v \rangle_{eff} = \sum_{c \text{ channels}} \langle \sigma v \rangle_c N_c \tag{3.4}$$

$$= \langle \sigma v \rangle_{tot.} \sum_{c \text{ channels}} \mathrm{BR}(\overline{X}X \to c) N_c \tag{3.5}$$

where $\langle \sigma v \rangle_{tot.}$ is the total dark matter annihilation cross section.

The total photon signal N_S is given by

$$N_S = \frac{1}{8\pi m_\chi^2} \bar{J}^{ann.} (I_{exp} \Delta\Omega) \sum_{c \text{ channels}} \langle \sigma v \rangle_c N_c \tag{3.6}$$

$$= \frac{\langle \sigma v \rangle_{tot.}}{8\pi m_\chi^2} \bar{J}^{ann.} (I_{exp} \Delta\Omega) \sum_{c \text{ channels}} \mathrm{BR}(\overline{X}X \to c) N_c \tag{3.7}$$

where $\bar{J}^{ann}$ is the average DM annihilation J-factor of the target, I_{exp} is the exposure and $\Delta\Omega$ is the solid angle subtended by the target. One can easily compute N_c in the parent particle frame for each channel, and then boosting the resulting spectrum back to the lab frame. The details by which we do this are outlines in Appendix A.4, and the results of these

calculations are shown in Table 3.2. Now, to calculate the photon signal N_S exactly is a model dependent endeavor, since one would need to calculate the DM branching ratios into each mesonic final state c. However, we can treat the branching ratios and total annihilation cross section as free parameters and obtain an estimate on its bound, which is what we will do in Section 3.7. It will be convenient to define

$$\Theta_{diff} := \bar{J}^{ann}_{diff} \frac{I_{exp} \Delta\Omega_{diff}}{8\pi m_\chi^2} \sim 1.4 \times 10^{33} \text{ cm}^{-3} \text{ s} \tag{3.8}$$

$$\Theta_{draco} := \bar{J}^{ann}_{draco} \frac{I_{exp} \Delta\Omega_{draco}}{8\pi m_\chi^2} \sim 2.2 \times 10^{29} \text{ cm}^{-3} \text{ s} \tag{3.9}$$

and label the states by an index (shown in Table 3.2). The predicted photon signal can then be expressed as

$$N_S = \Theta N_4 \langle \sigma v \rangle_{tot} \left(\text{BR}_4 + \sum_c n_c \text{BR}_c \right) \tag{3.10}$$

where $n_c = N_c/N_4$. Note that since $\sum_c \text{BR}_c = 1$ it follows that $\text{BR}_4 + \sum_c n_c \text{BR}_c < 1$, and so the maximum photon signal N_S^{max} is a pure function of the total cross section

$$N_S^{max} = \Theta N_4 \langle \sigma v \rangle_{tot} \tag{3.11}$$

In Section 3.7 we use (3.11) to obtain a general bound on the total DM annihilation cross section for both Draco and the diffuse emission.

3.5 The Application of Chiral Perturbation Theory to Dark Matter Interactions With Axial Currents

Since the coupling of dark matter to the light mesons is fundamentally governed by QCD and the dark matter-quark current contact interaction, we expect this interaction to exist at lower energies as well wherein the DM couples to the quark-confined states (mesons). At the CM energies we consider it is viable to express this interaction using the chiral Lagrangian formalism, in which the dark matter appears as an axial-vector spurion a_μ which, in general, breaks the approximate Standard Model flavor symmetry. We follow a similar approach to that followed in [10, 42].

Channel c	N_c	index
$\pi^0\pi^+\pi^-$	0.53	1
$\pi^0\pi^0\pi^0$	1.58	2
$\pi^0(\pi^-)^2(\pi^+)^2$	0.83	3
$(\pi^0)^3\pi^-\pi^+$	2.42	4

Table 3.2: Table of all accessible dark matter annihilation final states c. The N_c column is the average number of observed photons, given that the final state on the left is produced. The index is simply to assign an arbitrary ordering to the final states c.

Now, in order to describe the dark matter axial interaction with the quarks at energies below the confinement scale, we need to write down all operators allowed by the symmetries. We use the chiral Lagrangian formalism, which is just a convenient parametrization of all such operators. Our expansion parameter is $p/\Lambda_{QCD} \sim 0.7$, which isn't as small as one might dream. Therefore, we will also consider orders of the chiral Lagrangian beyond lowest order (3.12).

At lowest order, the chiral Lagrangian is

$$\mathcal{L}^{(2)} = \frac{f^2}{4} \mathrm{Tr}\left[D_\mu U \left(D^\mu U\right)^\dagger\right] \tag{3.12}$$

where

$$D_\mu U = \partial_\mu U - i\{a_\mu, U\} \tag{3.13}$$

$$U = e^{\frac{i\sqrt{2}}{f}\Phi} \tag{3.14}$$

$$\Phi = \frac{\lambda^a}{\sqrt{2}}\pi^a(x) = \begin{pmatrix} \frac{\pi^0}{\sqrt{2}} + \frac{\eta_8}{\sqrt{6}} & \pi^+ & K^+ \\ \pi^- & -\frac{\pi^0}{\sqrt{2}} + \frac{\eta_8}{\sqrt{6}} & K^0 \\ K^- & \bar{K}^0 & -\frac{2\eta_8}{\sqrt{6}} \end{pmatrix} \tag{3.15}$$

$$a^\mu \equiv \begin{pmatrix} a_u^\mu & 0 & 0 \\ 0 & a_d^\mu & 0 \\ 0 & 0 & a_s^\mu \end{pmatrix}. \tag{3.16}$$

and the pion decay constant is $f \sim 92$ MeV. Expanding U in equation (3.12) we obtain the order p and p^2 contributions to the Feynman rules for the final states listed in Table 3.1. The Feynman rules thereby obtained at this order are given below.

The next highest order chiral Lagrangian contains the order p^3 and p^4 contributions to the Feynman rules, and is given by

$$\begin{aligned}\mathcal{L}^{(4)} &= L_1 \,\mathrm{tr}\left[(D_\mu U)^\dagger D_\mu U\right]^2 \\ &+ L_2 \,\mathrm{tr}\left[(D_\mu U)^\dagger D_\nu U\right] \mathrm{tr}\left[(D^\mu U)^\dagger D^\nu U\right] \\ &+ L_3 \,\mathrm{tr}\left[(D_\mu U)^\dagger D^\mu U \,(D_\nu U)^\dagger D^\nu U\right] \\ &- i L_9 \,\mathrm{tr}\left[V^{\mu\nu}\left[(D_\mu U)^\dagger D_\nu U - D_\mu U \,(D_\nu U)^\dagger\right]\right] \end{aligned} \tag{3.17}$$

where

$$V_{\mu\nu} = \partial_\mu a_\nu - \partial_\nu a_\mu \tag{3.18}$$

and L_1, L_2, L_3, L_9 are phenomenologically measured dimensionless constants of order $\mathcal{O}(10^{-3})$.

Now, this Lagrangian $\mathcal{L}^{(4)}$ only corrects processes involving 3 or more final-state mesons, since at lowest order in Φ we have that $\mathcal{O}(|DU|^2) \sim \mathcal{O}(\Phi^2) + \mathcal{O}(a_\mu \Phi)$ and hence $\mathcal{O}(|DU|^4) \sim \mathcal{O}(\Phi^4) + \mathcal{O}(a_\mu \Phi^3)$, where we have dropped terms of order $\mathcal{O}(a_\mu^2)$. We note also that, at lowest order we get $\mathcal{O}(|DU|^6) \sim \mathcal{O}(\Phi^6) + \mathcal{O}(a_\mu \Phi^5)$, so the next order chiral Lagrangian will indeed contain corrections to our 5-meson final states. These corrections goes as $C_6 \left(p/\Lambda_{QCD}\right)^5 \sim C_6 \cdot 0.15$, where C_6 is a constant of dimension $[-2]$ introduced by the $\mathcal{O}(p^6)$ chiral Lagrangian $\mathcal{L}^{(6)}$. It has been shown in [40] that these constants are of order $\mathcal{O}(C_6) \sim 10^{-8}\mathrm{MeV}^{-2}$, which therefore gives us license to ignore these $\mathcal{O}(p^6)$ corrections. For the remainder of this paper, we take Lagrangains (3.12) and (3.17) to be the complete description of a dark matter axial current coupled to quarks at $\sqrt{s} \sim 700$ MeV. We note that, contrary to [42] it's not necessary to treat the DM branching fractions as free parameters, although we do this analysis anyhow. Rather, in our case the dark matter is sufficiently light to justify a perturbative treatment

of the chiral Lagrangian and take the tree level vertices as reliable estimates of the Feynman rules.

The details of the expansion of the chiral Lagrangian into its constituent meson fields and their corresponding Feynman rules are given in Appendix B.1. Some notable results from this expansion are that each of our Lagrangians is directly proportional to α_{ud}/Λ^2, and hence the Feynman rule corresponding to each channel is also proportional to α_{ud}/Λ^2. Obtaining a coupling of this form is to be more-or-less expected from the symmetry and kinematic arguments we made in Section 3.3. Kinematically, the coupling α_s corresponds to the dark matter interactions with the heavier scalar mesons (i.e. those composed of at least one strange quark) which are inaccessible at the CM energies we consider and so we expect all of the relevant couplings to go as $\alpha_u \pm \alpha_d$.

3.6 Photon Spectra & Comparison To Observations

In certain models or at higher CM energies like those in [42],[10], the photon spectrum can be the result of a multistep decay processes of intermediate mesons (e.g. Kaons, Vector Mesons) before finally producing photons. In our case however, the only kinematically accessible final states are those listed in Table 3.1, which are all DM contact interactions. Consequently, the only accessible photon producing final state meson is the π^0, which decays to two photons essentially 100% of the time. We neglect the $\pi^\pm$ photon production since the $\pi^\pm \to \gamma$ branching ratio essentially zero ($\lesssim 10^{-5}$ %).

In Figure 3.1 we show the photon spectrum obtained through the production of neutral pions produced from dark matter annihilation, assuming that $\sqrt{s} \sim 700$ MeV. The individual spectra have been normalized to the number of photons produced (i.e. two times the number of pions). In our calculations each spectrum is weighted according to their branching frac-

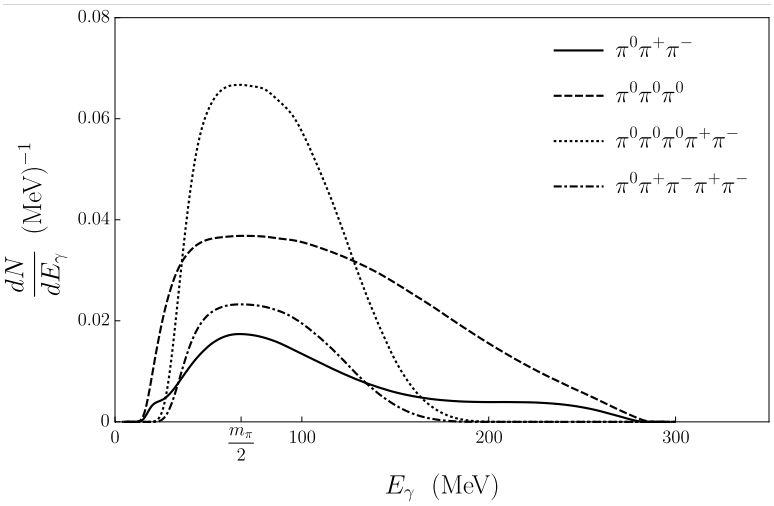

Figure 3.1: Photon spectrum for all kinematically accessible final states. The center of mass energy has been taken to be 700 MeV.

tions, though this is not shown in Figure 3.1. As is discussed in Appendix A.4, the photons produced by π^0 decay yield a signal with a peak at $m_\pi/2$ which smear out when boosting back to the lab frame, which can be seen in Figure 3.1.

Following [10], we consider constraints on the model from observations of diffuse photon emission, and from future observations of photon emission from the Draco dSph. We will take as a benchmark, an experiment with a fractional 1σ energy resolution of $\epsilon = 0.3$ and an exposure of $I_{exp} = 3000$ cm^2 yr.

For the diffuse emission, we restrict our attention to latitudes greater than 20°. In this region, and in the energy range $0.8\ \text{MeV} - 1\ \text{GeV}$, the isotropic flux observed by COMPTEL and EGRET can be well fit [4, 21] to the function

$$\frac{d^2\Phi^{iso.}}{d\Omega\ dE_{obs.}} = 2.74 \times 10^{-3} \left(\frac{E_{obs.}}{\text{MeV}}\right)^{-2.0} \text{cm}^{-2}\text{s}^{-1}\text{sr}^{-1}\text{MeV}^{-1}. \tag{3.19}$$

The expected number of observed events N_O between the energies E_- and E_+ is therefore

given by

$$N_O \;=\; 8.6\times 10^4 \left(\frac{\text{MeV}}{E_-}-\frac{\text{MeV}}{E_+}\right)\frac{(I_{exp.}\Delta\Omega)}{\text{cm}^2\ \text{yr sr}}. \tag{3.20}$$

Since our predicted signal peak is at $m_\pi/2$, we will consider a bin of photon energies centered at $E_0 = m_\pi/2$. and a width of $0.3E_0$ That is, we consider an energy bin between $E_- = (m_\pi/2)(1-\epsilon)$ and $E_+ = (m_\pi/2)(1+\epsilon)$.

To get an estimate on the constraints imposed on our model from diffuse emission, we impose that within this energy bin the number of expected signal events N_S not exceed the number of observed events. That is, we impose that we must have that $N_S < N_O$ in order for the model to be consistent with current observations from diffuse emission.

Now, when obtaining constraints that would be derived from future observations of a dense dark matter region such as the Draco dSph, the relevant quantity to consider is a statistically significant observation of the model's predicted value of N_S. As noted in Section 3.6, even in the absence of a photon signal due to DM annihilation there are background photon fluctuations of order $\sigma \sim \sqrt{N_O^{draco}}$, and so it makes sense take this to be our estimated uncertainty. We can therefore rule out a model that predicts a signal N_S at 5σ confidence if in a future observation no such $N_S > 5\sigma$ excess is detected. Absent of new information about the background emission that could improve resolution, this automatically renders searches for models which predict $N_S < 5\sigma$ inconclusive. If however such a $N_S > 5\sigma$ photon excess is detected upon future observations of Draco, then using (3.28) we can obtain an estimate on the minimum total DM annihilation cross section consistent with such an observation. Together these constraints provide upper and lower bounds and hence a range of cross sections consistent with a 5σ Draco photon excess and the diffuse emission.

3.6.1 Calculation of DM annihilation photon signal N_S

In this section we briefly outline how we go about calculating the predicted photon signal from DM annihilation N_S from the total DM annihilation cross section, for both the diffuse emission and the Draco case. In general differential photon flux from dark matter annihilation is given by

$$\frac{d^2\Phi}{d\Omega\, dE_\gamma} = \frac{\langle\sigma v\rangle}{8\pi m_\chi^2}\bar{J}^{ann}\frac{dN_\gamma}{dE_\gamma} \tag{3.21}$$

where $\bar{J}$ is the average J-factor of the target for dark matter annihilation, which accounts for the geometry and DM distribution of the target. The average J-factor for diffuse emission [27] and for Draco [22] are given by

$$\bar{J}^{ann}_{dif.} = 3.5 \times 10^{21}\ \mathrm{GeV}^2\ \mathrm{cm}^{-5}\mathrm{sr}^{-1} \tag{3.22}$$

$$\bar{J}^{ann.}_{Draco} = 6.94 \times 10^{21}\ \mathrm{GeV}^2\ \mathrm{cm}^{-5}\mathrm{sr}^{-1} \tag{3.23}$$

We account for instrumental energy resolution by convolving the injected photon spectrum with a Gaussian smearing function

$$R_\epsilon(E_{obs.}, E_\gamma) \;=\; \frac{1}{\sqrt{2\pi}\epsilon E_\gamma}\exp\left(-\frac{(E_{obs.}-E_\gamma)^2}{2\epsilon^2 E_\gamma^2}\right). \tag{3.24}$$

Now, in terms of the exposure I_{exp} and the solid angle of the target $\Delta\Omega$, the number of

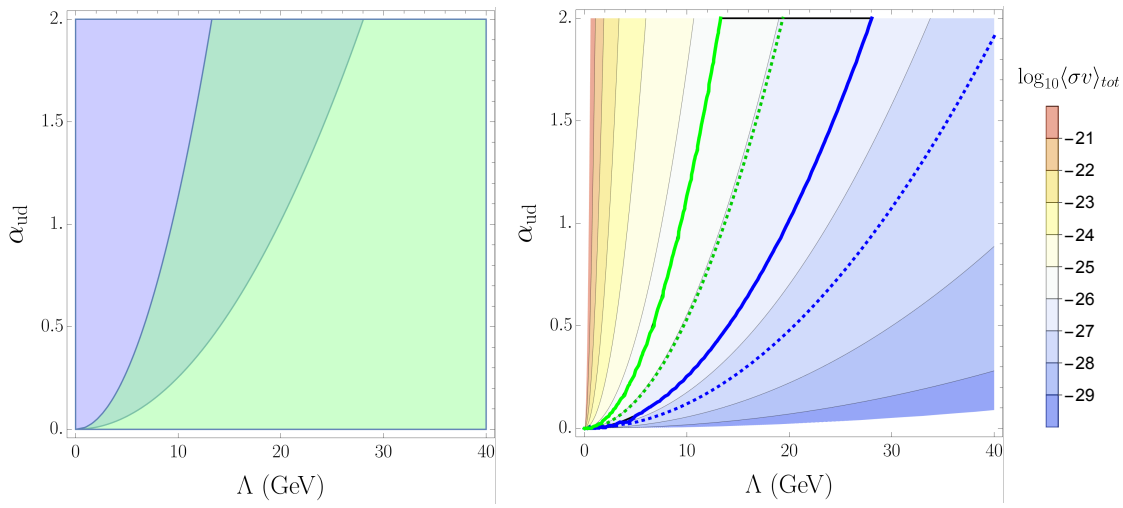

Figure 3.2: **(Left)** Constraints on parameter space induced purely from the results obtained from the chiral Lagrangian. Shown are the regions of parameter space consistent with observations from the diffuse emission (green) and a future 5σ photon excess from Draco (blue). **(Right)** Density plot of how the total DM annihilation cross section obtained from the chiral Lagrangian varies with the model parameters α_{ud}, Λ. The two dotted contours are the curves in parameter space which correspond to the total DM annihilation cross sections obtained from the coarse analysis in Section 3.7.

photons expected within the energy window $E_- \leq E_{obs} \leq E_+$ is therefore given by

$$N_S = \frac{\Xi}{8\pi m_\chi} \bar{J}^{ann}(I_{exp}\Delta\Omega) \int_{E_-}^{E_+} dE_{obs} \int_0^\infty dE_\gamma \frac{dN_\gamma}{dE_\gamma} R_\epsilon(E_{obs}, E_\gamma) \tag{3.25}$$

3.7 Results

We first consider the constraints imposed on the chiral Lagrangian description of our model. Recall that the vertices for each of the kinematically accessible final states are proportional to α_{ud}/Λ^2, and so the entire photon spectrum will be proportional to α_{ud}^2/Λ^4 and have no dependence on α_s. This is convenient as it allows us to completely explore the parameter space of both α_{ud} and Λ to find the combinations which are consistent with current and future observations, which we now do.

The bounds imposed on the model's parameter space by a future Draco search and current observations of the diffuse emission are shown in Figure 3.2 (left). As mentioned earlier, we have set the center of mass energy to be $\sqrt{s} = 2m_\chi \sim 700$ MeV. The parameter space consistent with a Draco 5σ photon excess provides a lower bound on the total DM annihilation cross section, and that the constraints induced by the diffuse emission provides an upper bound. The region overlap is our region of interest, as it is the region of parameter space which must be occupied by the model to qualify as a significant finding. That is, the region of parameter space consistent with both a Draco 5σ photon excess and current the diffuse emission observations is given by all of the (Λ, α_{ud}) that fall within the region of overlap between the two regions. This overlap region bound by two contours of constant cross section, defined by

$$2.10 \times 10^{-27} \ \frac{\text{cm}^3}{\text{s}} \ \lesssim \langle \sigma v \rangle_{tot} \ \lesssim \ 4.18 \times 10^{-26} \ \frac{\text{cm}^3}{\text{s}}. \tag{3.26}$$

We now consider the constrains imposed on our model that are obtained from our coarse estimates of the cross section (3.11). Recall that, as a function of the total DM annihilation cross section, we have found that the predicted photon signal due to DM annihilation can be no larger than

$$(N_S^{max})_{diff} = \Theta_{diff} N_4 \langle \sigma v \rangle_{tot} = \langle \sigma v \rangle_{tot} (3.4 \times 10^{33} \ \text{cm}^{-3} \ \text{s}) \tag{3.27}$$

$$(N_S^{max})_{draco} = \Theta_{draco} N_4 \langle \sigma v \rangle_{tot} = \langle \sigma v \rangle_{tot} (5.4 \times 10^{29} \ \text{cm}^{-3} \ \text{s}) \tag{3.28}$$

Note that these values were obtained with no mention to a chiral Lagrangian, as the only

necessary ingredients were a complete list of the possible final states of DM annihilation (which we found from symmetries). Nevertheless, we can still use these quantities to estimate the actual photon signal and thereby estimate the total annihilation cross section as well. We can then compare the estimates to those obtained from the chiral Lagrangian and provide an error estimate. Such estimates could be useful to future dark matter research for models where the final states are known but a Lagrangian description is either not possible or readily available.

Now, for the diffuse case we again apply the condition that the total predicted photon signal be consistent with the diffuse photon emission. Translating this constraint on the photon signal directly to an upper bound on the total DM annihilation cross section via Equation 3.27, we find that

$$\langle \sigma v \rangle_{tot} \lesssim 9.23 \times 10^{-27} \ \frac{\mathrm{cm}^3}{\mathrm{s}} \tag{3.29}$$

is the largest allowed cross section consistent with observations of the diffuse photon emission.

We now consider the lower bound on the total DM annihilation cross section that would be imposed by a 5σ photon excess from Draco. Now, the minimum photon signal N_S consistent with a 5σ photon excess occurs when $N_S = 5\sqrt{N_O^{draco}}$. Now, using Equation 3.28 to convert this into a bound on the total DM annihilation cross section we find that the lower bound is given by

$$\langle \sigma v \rangle_{tot} \gtrsim 4.64 \times 10^{-28} \ \frac{\mathrm{cm}^3}{\mathrm{s}}. \tag{3.30}$$

We visualize these findings in Figure 3.2 (right). Therein we show how the bound obtained via our coarse estimates of the cross sections (3.29), (3.30) relates to the cross sections obtained from the more precise description of the chiral Lagrangain. The green contours represent the upper bounds on the cross section by imposing that the dark matter signal be consistent with current observations of the diffuse emission, and the blue contours represent the lower bounds on the annihilation cross section consistent with a Draco 5σ photon excess. The solid lines are the predictions obtained from the chiral Lagrangian, and the dotted lines are the predictions obtained from the coarse estimates of the photon signal (3.27) and (3.28).

Looking at Figure 3.2 (right), we see that our Lagranian-free coarse estimates on the total DM annihilation cross section admit a region in parameter space that is larger and centered around a smaller total cross section than that obtained from the chiral Lagrangian. Specifically, the constraints induced on the total DM annihilation cross section from both analyses are

$$4.64 \times 10^{-28} \ \frac{\text{cm}^3}{\text{s}} \ \lesssim \langle \sigma v \rangle_{tot} \ \lesssim \ 9.23 \times 10^{-27} \ \frac{\text{cm}^3}{\text{s}} \qquad \text{(Coarse Estimates)} \tag{3.31}$$

$$2.10 \times 10^{-27} \ \frac{\text{cm}^3}{\text{s}} \ \lesssim \langle \sigma v \rangle_{tot} \ \lesssim \ 4.18 \times 10^{-26} \ \frac{\text{cm}^3}{\text{s}} \qquad \text{(Chiral Lagrangian).} \tag{3.32}$$

Note that this particular trend of discrepancies is expected of our estimates. For both cases of Draco and the diffuse spectrum, the estimate on the predicted signal N_S^{max} relates to the predicted signal obtained from the chiral Lagrangian N_S via

$$N_S = N_S^{max} \left(\text{BR}_4 + \sum_c n_c \text{BR}_c \right) < N_S^{max} \tag{3.33}$$

So when we fix $N_S = N_O$ from the chiral Lagrangian, we expect that to correspond to a larger $\langle \sigma v \rangle_{tot}$ than what we obtain when we fix $N_S^{max} = N_O$, since the former is suppressed by the sum over the branching ratios. Therefore, we expect the total annihilation cross section obtained from the coarse estimates to be smaller for both Draco and the diffuse emission, which is exactly what we see in Figure 3.2.

3.8 Conclusions

In conclusion, we have considered dark matter which communicates to the Standard Model via coupling directly to the quarks as an axial-vector current of the form $\alpha_q a_\mu (\overline{q}\gamma^\mu\gamma^5 q)$. We have argued the set of all possible mesonic final states resulting from DM annihilation from kinematics and symmetry considerations. Moreover, we have also found the set of all final states by way of the chiral Lagrangian description of the DM-quark coupling at energies below the confinement scale, which is in agreement with our arguments from symmetry. From these final states we found the photon spectrum for dark matter annihilation.

In this work we have found that current observations of the diffuse photon background emission can already be used to obtain an upper bound on the total dark matter annihilation cross section in a Lagrangian-free manner, as well as the model parameters themselves when using the chiral Lagrangian description. Furthermore, we have found that future observations of dwarf spheroidal galaxies (dSphs) will significantly refine the bounds on the model's parameter space (or possibly discover this model), as it provides a lower bound on the total dark matter annihilation cross section.

Chapter 4

Dark Matter Freeze Out during an Early Cosmological Period of QCD Confinement

This chapter heavily relies on previously published work in collaboration with Tim M.P Tait., Seyda Ipek and Michael Waterbury [74].

4.1 Introduction

In this chapter, we explore a different kind of nonstandard cosmology, in which the strong interaction described by Quantum Chromodynamics (QCD) undergoes an early phase of confinement, based on promoting the strong coupling α_s to a field, whose potential receives thermal corrections which cause it to take larger values at early times, relaxing to the canonical size some time before BBN [48, 49]. If the dark matter freeze out occurs during a period in which α_s is larger such that QCD is confined, the degrees of freedom of the Universe

are radically different from the naive extrapolation, being composed largely of mesons and baryons rather than quarks and gluons. Similarly, the interactions of the dark matter with the hadrons are scaled up by the larger QCD scale, $\Lambda_{\rm QCD}$, leading to a very different annihilation cross section at the time of freeze-out than during the epoch in which experimental bounds are operative. We find that depending on the underlying form of the dark matter interactions with quarks, radical departures from the expected relic density are possible.

This chapter is organized as follows. In Section 4.2, we review the construction of a Universe in which α_s varies with temperature. In Section 4.3 we discuss the chiral perturbation theory which describes the mesons and their interactions with the dark matter during the period of early confinement, and in Section 4.4, we examine the relic density under different assumptions concerning α_s at the time of freeze-out, and contrast with experimental constraints derived today. We reserve Section 4.5 for our conclusions and outlook.

4.2 Early QCD Confinement

Following reference [48], we modify the gluon kinetic term in the SM Lagrangian to:

$$-\frac{1}{4g_{s0}^2}G^a_{\mu\nu}G_a^{\mu\nu} \quad \Rightarrow \quad -\frac{1}{4}\left(\frac{1}{g_{s0}^2}+\frac{S}{M_*}\right)G^a_{\mu\nu}G_a^{\mu\nu}\ , \tag{4.1}$$

where $G^a_{\mu\nu}$ is the gluon field strength, S is a gauge singlet real scalar field, and g_{s0} represents (after rescaling the kinetic term to canonical normalization) the $SU(3)$ gauge coupling in the absence of a vacuum expectation value (VEV) for S. M_* is a parameter with dimensions of energy which parameterizes a non-renormalizable interaction between S and the gluons. It could represent the fluctuations of a radion or dilaton field, or by integrating out heavy vector-like $SU(3)$-charged particles which also couple to the scalar field S. In the latter case, the scale of the interaction is related to the mass of the new $SU(3)$-charged particles via

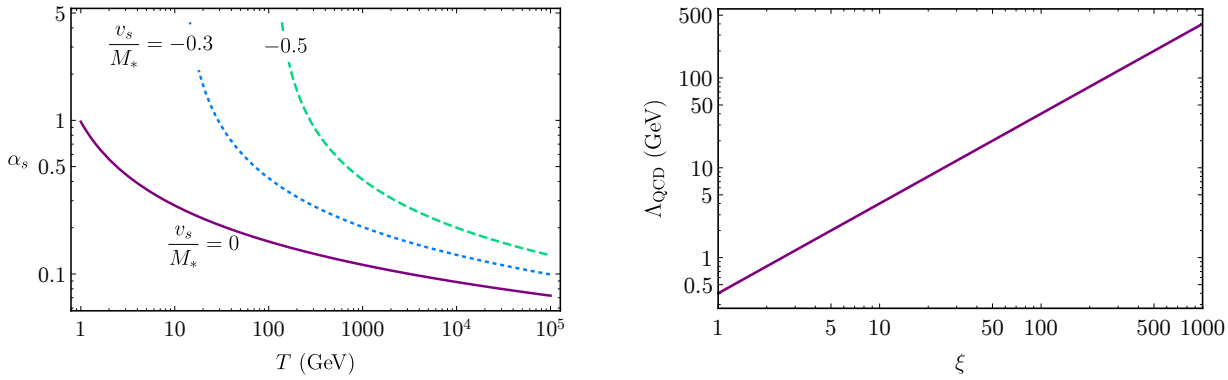

Figure 4.1: **Left panel:** Evolution of the strong coupling constant with temperature in the early Universe for three different values of v_s/M_*. Confinement takes place at temperatures for which $\alpha_s \gg 1$. **Right panel:** The scale of QCD confinement, $\Lambda_{\rm QCD}$, as a function of the parameter $\xi = \exp(24\pi^2/(2N_f - 33)v_S/M_*)$.

$M_* \sim 4\pi M_Q/n_Q y_Q \alpha_s$, where n_Q is the number of $SU(3)$-charged fermions with mass M_Q and Yukawa coupling y_Q.

Engineering an early period of confinement, followed by subsequent deconfinement and return to a SM-like value of α_s before BBN imposes constraints on the potential for S, and its interactions with other fields (which determine the thermal corrections to its potential) [48]. Generally, mixed potential terms containing the SM Higgs doublet are present, and these may play an important role in the thermal history [49]. In this work, we remain agnostic concerning the specific dynamics which implement the shift in v_S leading to early confinement, and we assume that the terms mixing the S with the SM Higgs are small enough so as to be safely neglected.

A VEV for S generates a non-decoupling correction to the effective strong coupling constant through the dimension-5 interaction in (4.1), which for negative v_s strengthens the effective coupling strength. At one loop and at scale μ, the effective strong coupling is

$$\frac{1}{\alpha_s(\mu, v_s)} = \frac{33 - 2N_f}{12\pi} \ln\left(\frac{\mu^2}{\Lambda_0^2}\right) + 4\pi \frac{v_s}{M_*}, \tag{4.2}$$

where N_f is the number of active quark flavors at the scale $\mu \sim T$. (4.1) shows the effective

coupling as a function of temperature. QCD confinement occurs at a temperature $T_c \simeq \Lambda_{\rm QCD}$, where

$$\Lambda_{\rm QCD}(v_s) = \Lambda_{\rm QCD}^{\rm SM}\, e^{\frac{24\pi^2}{2N_f-33}\frac{v_s}{M_*}}. \tag{4.3}$$

Here, $\Lambda_{\rm QCD}^{\rm SM} \simeq 400$ MeV is the SM value of the QCD confinement scale; we adjust g_{s0} such that it is realized for $v_s = 0$.

At scales below confinement, the relevant degrees of freedom are mesons, whose dynamics are described by chiral perturbation theory, the effective field theory of which is parameterized by coefficients which depend on $\Lambda_{\rm QCD}$. We find it convenient to parameterize the physics in terms of the ratio of $\Lambda_{\rm QCD}$ to $\Lambda_{\rm QCD}^{\rm SM}$,

$$\xi \equiv \frac{\Lambda_{\rm QCD}}{\Lambda_{\rm QCD}^{\rm SM}} \simeq \exp\left(\frac{24\pi^2}{2N_f-33}\frac{v_s}{M_*}\right). \tag{4.4}$$

The parameter ξ is typically sufficient to completely describe the physics of dark matter interactions during the period of early confinement.

4.3 Dark Matter Interactions and Chiral Perturbation Theory

The dynamics of the scenario we study are encoded in the Lagrangian:

$$\mathcal{L} \supset -\frac{1}{4}\left(\frac{1}{g_{s0}^2}+\frac{S}{M_*}\right) G^a_{\mu\nu}G_a^{\mu\nu} + \sum_q \left\{ i\bar{q}\not{D}q - y_q\, h\bar{q}_L q_R + \text{H.c.}\right\} + \mathcal{L}_\chi\,, \tag{4.5}$$

where $\mathcal{L}_\chi$ describes the dark matter and its interactions. We introduce a SM-singlet Dirac fermion field χ to represent the dark matter, and couple it to quarks,

$$\mathcal{L}_\chi = i\bar{\chi}\gamma^\mu\partial_\mu\chi - m_\chi\bar{\chi}\chi + \sum_{\bar{i},j}\left\{\frac{\beta_{ij}}{M_S^2}\bar{\chi}\chi\ \bar{q}_i q_j + \frac{\lambda_{ij}}{M_V^2}\bar{\chi}\gamma^\mu\chi\ \bar{q}_i\gamma_\mu q_j\right\}, \tag{4.6}$$

where the couplings β_{ij}/M_S^2 and λ_{ij}/M_V^2 represent operators left behind by integrating out states with masses $\gg m_\chi$. Generically, one would also expect there to be interactions with the leptons or the Higgs doublet. We assume for simplicity that such interactions are subdominant if present.

In the case of the scalar interactions, S itself could act as the mediator, provided it has direct coupling to the dark matter. In that case, UV-completing will require additional states to provide a renormalizable portal to $h\bar{q}q$, and the dimension six interaction written here will descend from a dimension seven operator after the SM Higgs gets its VEV. The vector interactions could represent a Z' from an additional U(1) gauge symmetry that couples to both quarks and dark matter. We will consider cases in which either scalar or vector interactions dominate over the other one. We follow the guidance of minimal flavor violation [66] in choosing the couplings such that

$$\beta_{ij} \equiv \pm\delta_{ij}\frac{y_i}{y_u}, \tag{4.7}$$

which is normalized to the coupling to up quarks, and with an over-all factor absorbed into M_S^2. The possibility of choosing either sign for β will play an important role, described in 4.21 below.

The vector couplings λ_{ij} are diagonal and have equal values for the up-type quarks, and

equal (but different from the up-type) values for the down-type quarks,

$$\lambda_{ij} \equiv \begin{cases} \delta_{ij}, & j = u, c, t \\ (1+\alpha)\delta_{ij}, & j = d, s, b \ , \end{cases} \tag{4.8}$$

where α determines the difference between up- and down-type couplings. When $\alpha = 0$, the vector coupling assigns charges equivalent to baryon number, and the mesons decouple from the dark matter.

During early confinement, the Universe looks very different from the standard cosmological picture based on the SM extrapolation. (Massless) quark and gluon degrees of freedom are replaced by mesons and baryons, and chiral symmetry breaking induces a tadpole for the Higgs which is relevant for the evolution of its VEV. In order to determine how dark matter interactions are affected by this early cosmological period of QCD confinement, we first give a description of this era in terms of chiral perturbation theory.

4.3.1 Chiral Perturbation Theory

In the limit $\Lambda_{\rm QCD} \gg m_t$, the QCD sector of the Lagrangian for quarks,

$$\mathcal{L} \supset \sum_q \left\{ i\bar{q}\not{D}q - y_q\, h \bar{q}_L q_R + \text{H.c.} \right\} \tag{4.9}$$

(where h is the SM Higgs radial mode) possesses an approximate global $\text{SU}(6)_L \times \text{SU}(6)_R$ chiral symmetry, which is softly broken by the Yukawa interactions. We work in the basis in which the y_q's are diagonal, for which all flavor-changing processes reside in the electroweak interactions. Non-perturbative QCD is expected to break $\text{SU}(6)_L \times \text{SU}(6)_R \to SU(6)_V$ to the diagonal subgroup, resulting in $6^2 - 1 = 35$ pions as pseudo-Nambu-Goldstone bosons.

At scales below $\Lambda_{\rm QCD}$, the pions are described by a nonlinear sigma model built out of

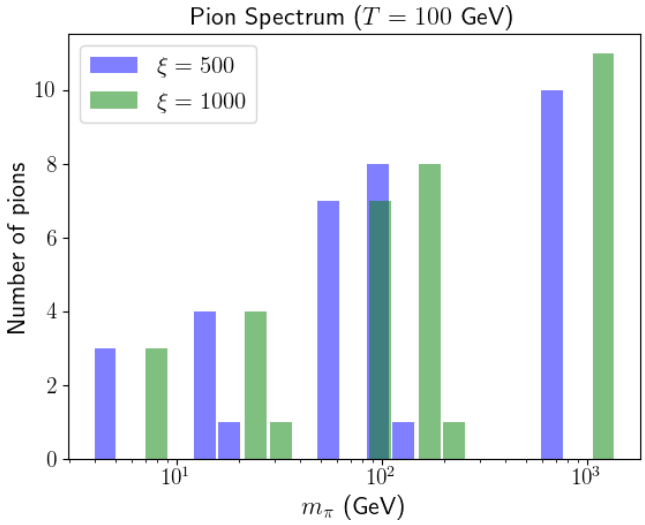

Figure 4.2: Spectrum of pion masses for two choices of ξ, with v_h corresponding to the Higgs VEV at $T = 100$ GeV.

$U(x) \equiv \exp\left(i2T^a\pi^a(x)/f_\pi\right)$, where T^a are the $SU(6)$ generators. The leading terms in the chiral Lagrangian (neglecting electroweak interactions) are

$$\mathcal{L}_{\text{ch}} = \frac{f_\pi^2}{4}\ \text{tr}(|D_\mu U|^2) + \kappa\ \ \text{tr}(U M_q^\dagger + M_q U^\dagger)\ , \tag{4.10}$$

where f_π is the pion decay constant and κ is a constant with mass dimension 3, both of which represent the strong dynamics. The generators are normalized such that $\text{tr}[T^a T^b] = \delta^{ab}/2$, leaving the π^a canonically normalized. The mass matrix M_q is a spurion representing the explicit $\text{SU}(6)_L \times \text{SU}(6)_R$ breaking from the Yukawa interactions,

$$M_q = \frac{1}{\sqrt{2}} h\ \text{Diag}(y_u, y_d, y_s, y_c, y_b, y_t)\ . \tag{4.11}$$

Expanding the field U in (4.10) to second order in π/f_π results in pion mass terms and a tadpole for the Higgs:

$$\mathcal{L}_{\text{ch}} \supset \sqrt{2}\kappa\, y_t\, h - \frac{\kappa}{f_\pi^2}\,\text{tr}[\{T^a, T^b\}M]\,\pi^a\pi^b\ , \tag{4.12}$$

both of which are controlled by κ. (In the tadpole term we keep only the top Yukawa as the contributions from light quarks are typically negligible.) We match f_π and κ to the SM pion mass, $m_{\pi 0} = 135$ MeV, and decay constant, $f_{\pi 0} = 94$ MeV at $\xi = 1$ and $v_h = v_h^0$, where $v_h^0 = 246$ GeV is the zero temperature SM Higgs VEV. Naive dimensional analysis provides the scaling for other values of ξ (for which the tadpole implies there will typically be a different v_h):

$$\kappa \simeq (220 \text{ MeV})^3 \, \xi^3 \, , \qquad f_\pi \simeq 94 \text{ MeV} \, \xi, \qquad m_\pi^2 \simeq m_{\pi 0}^2 \, \xi \, v_h / v_h^0, \tag{4.13}$$

The resulting pion mass matrix is diagonalized numerically to determine the spectrum of mesons in the mass basis. Example spectra at $T = 100$ GeV for two different choices of ξ are shown in Figure 4.2.

4.3.2 Finite Temperature Higgs Potential

As shown above, a cosmological era of early QCD confinement induces a tadpole for the Higgs radial mode h. If $\Lambda_{\rm QCD}$ is comparable in size to the weak scale, this tadpole can deform the Higgs potential by a relevant amount during the epoch of confinement. In addition, the plasma contains mesons (rather than quarks), which modifies the thermal corrections to the Higgs potential from the SM fermions.

We determine the Higgs VEV as a function of temperature by finding the global minimum of the finite-temperature Higgs potential. We assume that interaction terms between the Higgs and S are small enough to be neglected. We focus on a cosmological history where $\Lambda_{\rm QCD} > T_{\rm EW} \sim 150$ GeV, which requires $\xi \gtrsim 300$. We further assume that the S potential is such that there is a lower temperature T_d (which we treat as a free parameter) at which $\Lambda_{\rm QCD}$ returns to $\Lambda_{\rm QCD}^{\rm SM}$, implying that QCD deconfines and the subsequent evolution of the Universe is SM-like.

Under these assumptions, the finite temperature potential for the Higgs, $V(h,T)$ consists of the tree level SM potential,

$$V_0(h) = -\frac{1}{2}\mu^2 h^2 + \frac{\lambda}{4}h^4 \ , \tag{4.14}$$

whose parameters are adjusted to match the zero temperature VEV $v_h^0 = 246$ GeV and Higgs mass $m_h \simeq 126$ GeV. In three different temperature regimes, the form of the finite temperature corrections is given as

$$V(h,T) = \begin{cases} V_0(h) + \dfrac{T^4}{2\pi^2}\displaystyle\sum_{i=h,W,Z,t}(-1)^F n_i J_{B/F}\left[m_i^2/T^2\right] & (T > \Lambda_{\rm QCD}) \\ V_0(h) - \sqrt{2}\kappa y_t h + \dfrac{T^4}{2\pi^2}\displaystyle\sum_{i=h,W,Z,\pi^a} n_i J_B\left[m_i^2/T^2\right] & (T_d < T < \Lambda_{\rm QCD}) \ , \\ V_0(h) + \dfrac{T^4}{2\pi^2}\displaystyle\sum_{i=h,W,Z,t}(-1)^F n_i J_{B/F}\left[m_i^2/T^2\right] & (T < T_d) \ , \end{cases} \tag{4.15}$$

where $F = 0/1$ for bosons/fermions and n_i counts degrees of freedom: $n_h = n_\pi = 1$, $n_W = 6$, $n_Z = 3$, and $n_t = 12$. The functions $J_{B/F}$ are the bosonic/fermionic thermal functions,

$$J_{B/F}\left[m_i^2/T^2\right] = \int_0^\infty x^2 \log\left(1 - (-1)^F e^{-\sqrt{x^2 + m_i^2/T^2}}\right) \tag{4.16}$$

and $m_i^2(h)$ are the field dependent masses,

$$m_h^2 = -\mu^2 + 3\lambda h^2, \qquad m_W^2 = \frac{g_W^2}{4}h^2, \qquad m_Z^2 = \frac{g_W^2}{4\cos^2(\theta_w)}h^2, \qquad m_t^2 = \frac{y_t^2}{2}h^2. \tag{4.17}$$

We make use of the high temperature expansions of the thermal functions, which are given as

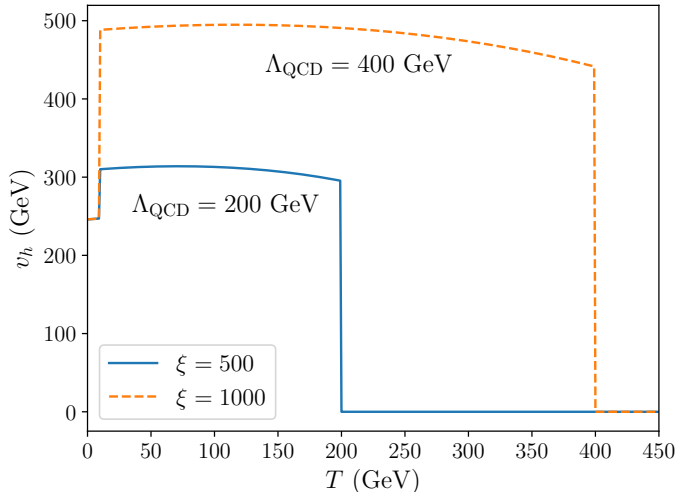

Figure 4.3: Higgs VEV as a function of temperature T for $\xi = 500, 1000$ and $T_d = 10$ GeV. The sudden changes occur at $T \simeq \Lambda_{\rm QCD}$ and T_d.

$$J_B\left(m^2(h)/T^2\right) = -\frac{\pi^4}{45} + \frac{\pi^2}{12}\frac{m^2(h)}{T^2} - \frac{\pi}{6}\left(\frac{m^2(h)}{T^2}\right)^{3/2} + \mathcal{O}\left[\frac{m^4}{T^4}\log\left(\frac{m^2}{T^2}\right)\right] ,$$
$$J_F\left(m^2(h)/T^2\right) = \frac{7\pi^4}{360} - \frac{\pi^2}{24}\frac{m^2(h)}{T^2} + \mathcal{O}\left[\frac{m^4}{T^4}\log\left(\frac{m^2}{T^2}\right)\right] . \tag{4.18}$$

The meson masses in the confined phase are calculated as described in the previous section. We find that for the values of ξ under consideration, the mesons containing top quarks are typically much heavier than the temperature during the period of early confinement such that they are Boltzmann suppressed. Hence the dominant thermal corrections are from the mesons containing bottom quarks. We keep all 35 mesons in our numerical calculations.

At high temperatures, the potential is dominated by the T^2h^2 term, driving $v_h \to 0$, and the electroweak symmetry is restored. At $T = \Lambda_{\rm QCD}$, chiral symmetry is broken via the quark condensate, and the tadpole triggers a non-zero Higgs VEV that is larger than v_h^0 for the ξ values we consider. At T_d, QCD deconfines and the Higgs VEV relaxes to its SM value. This behavior is shown in Figure 4.3 for $T_d = 10$ GeV and two values of ξ.

4.3.3 Dark Matter Interactions with pions

At leading order in chiral perturbation theory, the interactions with the dark matter map onto,

$$\frac{\kappa}{M_S^2}\ \bar{\chi}\chi\ \mathrm{tr}\left(U^\dagger\beta + U\beta^\dagger\right) + \frac{i}{M_V^2}\ \bar{\chi}\gamma^\mu\chi\ \mathrm{tr}\left((\partial_\mu U^\dagger)\ [\lambda, U] - [U^\dagger, \lambda^\dagger]\ (\partial_\mu U)\right)\ , \tag{4.19}$$

with κ and f_π determined as discussed in Section 4.3.1. Note that because the scalar interaction with dark matter is chosen to take the same form as the spurion containing the quark masses, a single hadronic coefficient κ determines both the pion masses and the dark matter couplings [67]. Expanding U to second order for Hermitian choices of β and λ produces:

$$\frac{2\kappa\ \mathrm{tr}\,[\beta]}{M_S^2}\ \bar{\chi}\chi + \frac{2\kappa}{f_\pi^2}\frac{1}{M_S^2}\ \mathrm{tr}[T^a T^b \beta]\ \bar{\chi}\chi\pi^a\pi^b + \frac{2i}{M_V^2} f^{abc}\ \mathrm{tr}[T^b\lambda]\ \bar{\chi}\gamma^\mu\chi\ \pi^a(\partial_\mu\pi^c)\,. \tag{4.20}$$

It is worth noting that the strength of the scalar interaction scales as $\kappa/f_\pi^2 \propto \xi$, whereas the vector-interaction strength is independent of it.

The first term in Equation (4.20) represents a contribution to the dark matter mass induced by the chiral condensate. At the time of freeze out, the effective mass is given by the sum of $m_\chi^{T=0}$, which to good approximation is m_χ in the Lagrangian (4.6), and this additional correction that is operative during confinement,

$$m_\chi^{T=T_F} = m_\chi^{T=0} + \Delta m_\chi\ , \quad \text{where}\ \ \Delta m_\chi \simeq (2\ \mathrm{eV})\,\xi^3 \left(\frac{10^6\ \mathrm{GeV}}{M_S}\right)^2\ . \tag{4.21}$$

For large values of ξ, the effective shift may be a few GeV, and may play a role in determining the relic abundance for dark masses of $O(10\ \mathrm{GeV})$. In (4.4) we present our results in terms of the $T = 0$ (unshifted) mass relevant for WIMP searches today. For dark matter masses of $O(\mathrm{GeV})$, the sign of the effective mass term may flip between the time of freeze out and today due to a sign difference between m_χ and β. For sufficiently complicated WIMP interactions,

this could lead to non-trivial interference effects, but for the simple cases we consider here it is unimportant.

4.4 Dark Matter Parameter Space

In this section, we consider dark matter freezing out through either the scalar or vector interactions introduced above during an early cosmological period of QCD confinement. We contrast with the expectations from a standard cosmology and constraints from direct searches.

4.4.1 Relic Density

The Boltzmann equation describing the evolution of the density of dark matter in an expanding Universe can be written as [68]:

$$\frac{dn_\chi}{dt} + 3Hn_\chi = -\langle\sigma v\rangle(n_\chi^2 - n_{eq}^2)\,, \tag{4.22}$$

where n_χ is the co-moving number density of the dark matter, and n_{eq} is its equilibrium density at a given temperature. When the interaction rate drops below the expansion rate of the Universe, H, the dark matter number density stabilizes, leaving a relic of the species in the Universe today. The relic density can be solved for a non-relativistic species with a thermally averaged cross section approximated as $\langle\sigma v\rangle \sim a + 6b/x$ where $x \equiv m_\chi/T$. The resulting relic density is:

$$\Omega_\chi h^2 \approx \frac{1.04\times10^9}{M_{Pl}}\frac{x_F}{\sqrt{g_*}}\frac{1}{a+3b/x_F}\,, \tag{4.23}$$

where g_* counts the number of relativistic degrees of freedom at freeze-out and h parameterizes the Hubble scale. For the standard case of $\xi = 1$, we have $g_* = 92$. In an era of QCD confinement at $T \sim 10 - 100$ GeV, the degrees of freedom changes from the standard scenario since quarks and gluons confine into (heavy) mesons. For the cases we study, this corresponds to $g_* \simeq 26$ at the time of dark matter freeze-out. The freeze out temperature $x_F = m_\chi / T_F$ can be solved for iteratively via

$$x_F = \ln \left(c(c+2) \sqrt{\frac{45}{8}} \frac{g_\chi}{2\pi^3} \frac{m_\chi M_{Pl}(a + 6b/x_F)}{\sqrt{g_* x_F}} \right) , \tag{4.24}$$

where $g_\chi = 2$ for fermionic dark matter and $c = 1/2$ approximates the numerical solution well [68]. The parameters a, b in the annihilation cross section are model dependent. We compute them in (**??**) for scalar and vector interactions, respectively.

The preceding discussion assumes that the freeze out takes place during a time of radiation domination, as is the case for a WIMP in the backdrop of a standard cosmology. It is generally expected that QCD confinement results in a shift in the vacuum energy of $c_0 \Lambda_{\rm QCD}^4$, where c_0 is a dimensionless constant which naive dimensional analysis would suggest is order 1. The relic density in Equation (4.23) assumes that the subsequent deconfinement of QCD occurs before the onset of vacuum domination,

$$\Lambda_{\rm QCD} \gtrsim T_F \gtrsim \Lambda_{\rm QCD} \left(\frac{c_0}{g_*} \right)^{1/4} . \tag{4.25}$$

For $c_0 \sim 1$, this is a relatively narrow range which would involve some fine-tuning between the freeze out temperature and $\Lambda_{\rm QCD}$ for Equation (4.23) to hold. However, the tiny value of the vacuum energy inferred from cosmic acceleration in the current era could argue that there is some mechanism at work which dynamically cancels the influence of vacuum energy in different epochs, which would allow for a much wider period of radiation domination.

4.4.2 Limits from Direct Searches

Direct detection experiments such as XENON provide important bounds on parameter space based on the null results for dark matter scattering with nuclei. The rate for χ to scatter with a nucleus N in the non-relativistic limit is,

$$\sigma_{\chi N} = \frac{1}{\pi}\frac{m_\chi^2 m_N^2}{(m_\chi + m_N)^2}[Z f_p + (A - Z) f_n]^2 \,, \tag{4.26}$$

where Z and A are the atomic number and mass number respectively and $f_{p/n}$ are the effective couplings to protons/neutrons, given by

$$\begin{aligned} &\text{Scalar Interaction}: f_{p/n} = \frac{1}{M_S^2}\left\{\sum_{q=u,d,s} f_{Tq}^{(p/n)} + \frac{2}{9} f_{Tg}^{(p/n)}\right\} \,, \\ &\text{Vector Interaction}: f_p = \frac{1}{M_V^2}(3+\alpha) \,, \quad f_n = \frac{1}{M_V^2}(3+2\alpha) \,, \end{aligned} \tag{4.27}$$

at leading order [71], with hadronic matrix elements f_{Tq}, and f_{Tg} defined as in references [69, 70].

4.4.3 Scalar-Mediator Results

It can be seen from (4.20) that the strength of scalar interaction between dark matter and pions depend on the QCD confinement scale, $\Lambda_{\rm QCD} = \xi \Lambda_{\rm QCD}^{\rm SM}$. Consequently, for dark matter with purely scalar interactions, the relic density is a function of the mediator scale M_S, QCD confinement scale $\Lambda_{\rm QCD}$, and the mass of the dark matter at zero temperature, $m_\chi^{T=0}$. We consider $\xi = 1, 500, 1000$, where $\xi = 1$ represents the standard cosmological history and the other two choices correspond to $\Lambda_{\rm QCD} = 200, 400$ GeV, respectively.

The relic abundance is controlled by the thermally-averaged annihilation cross section at the

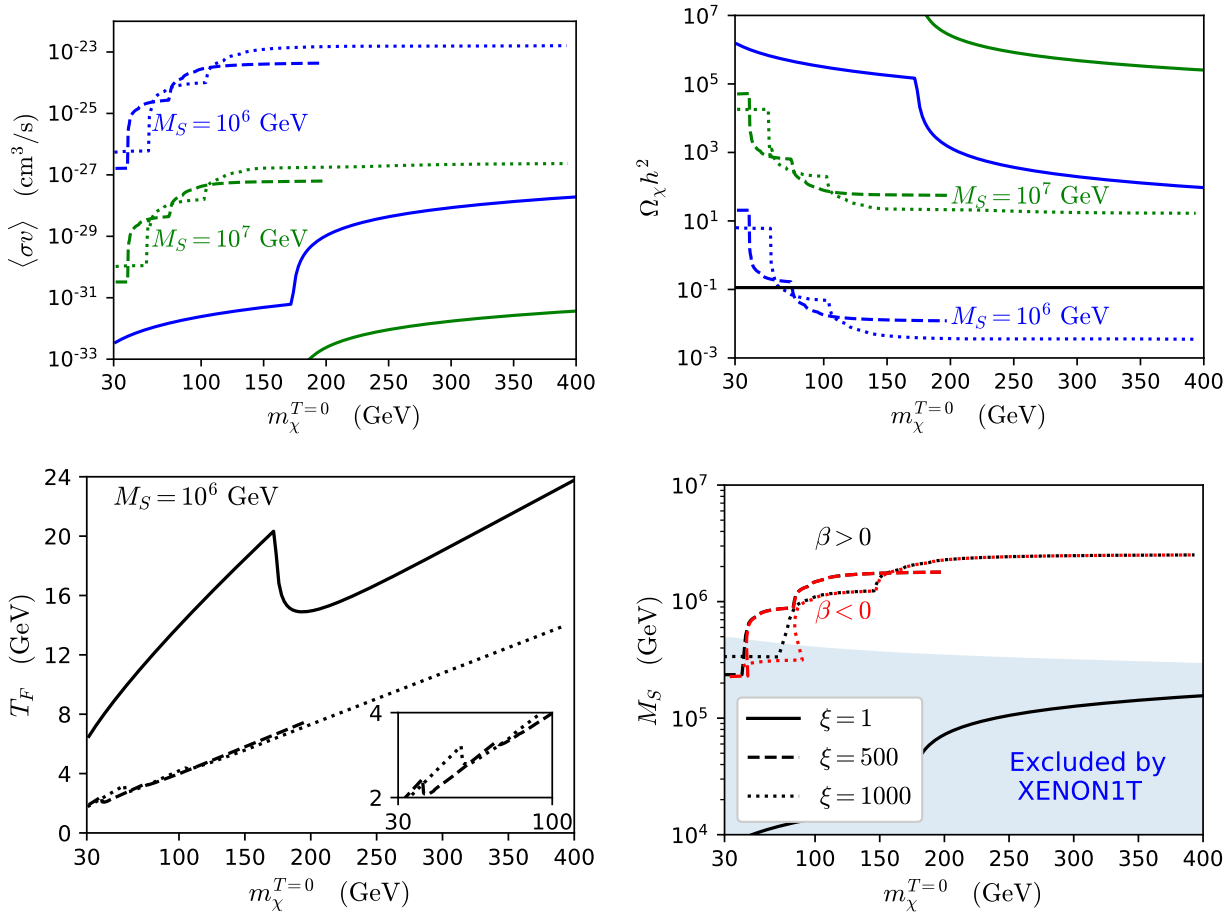

Figure 4.4: **(Top Left)** The thermally-averaged cross-sections at the time of freeze-out as a function of $m_\chi^{T=0}$ plotted for $M_S = 10^6$ GeV (blue), 10^7 GeV (green) and ξ =1 (solid), 500 (dashed), 1000 (dotted). **(Top Right)** Dark matter relic abundance today as a function of $m_\chi^{T=0}$ plotted for $M_S = 10^6$ GeV (blue), 10^7 GeV (green) and $\xi = 1, 500, 1000$. The horizontal solid line is the observed dark matter abundance. **(Bottom Left)** The freeze-out temperature T_F as a function of $m_\chi^{T=0}$ with $M_S = 10^6$ GeV, 10^7 GeV plotted for ξ =1 (solid), 500 (dashed), 1000 (dotted). **(Bottom Right)** We show the M_S values that produce the observed dark matter relic abundance as a function of $m_\chi^{T=0}$ for ξ =1 (solid), 500 (dashed), 1000 (dotted). For $\beta < 0$, the line is plotted in red. Shaded blue region is excluded by XENON1T. See text for details.

time of freeze out ($T = T_F$) in the non-relativistic limit,

$$\langle \sigma_S v \rangle = \left(\frac{\kappa}{f_\pi^2 M_S^2} \right)^2 \sum_{\pi_a} \frac{\omega_a^2}{4\pi} \sqrt{1 - \frac{m_{\pi_a}^2}{m_\chi^2}} \langle v^2 \rangle + \mathcal{O}(\langle v^4 \rangle) \ . \tag{4.28}$$

Here ω_a are the eigenvalues of the 35×35 matrix $\mathrm{tr}(T^a T^b \beta)$, and the sum is over all the

pions of mass[1] less than $m_\chi^{T=T_F}$. Note that scalar interactions lead to p-wave suppressed annihilation, for which $a = 0$. The relic abundance today is given by $\rho_\chi = m_\chi^{T=0} n_\chi$, whereas the energy density immediately after freeze out is $m_\chi^{T=T_F} n_\chi$. The shift in m_χ between the time of freeze out and the present epoch introduces an additional correction to the relic density today:

$$\Omega_\chi^{T=0} h^2 = \frac{m_\chi^{T=0}}{m_\chi^{T=0} + \Delta m_\chi} \Omega_\chi^{T=T_F} h^2. \tag{4.29}$$

In Figure 4.4, we show the annihilation cross section, relic density today, and freeze out temperature, for $\xi = 1, 500, 1000$ and two representative values of M_S, as a function of the dark matter mass today. In the final panel, we show the value of M_S for each dark matter mass (today) required to reproduce the observed relic density, for the same values of ξ considered. Also plotted on that panel are the current XENON1T constraints [50]. Comparing $\xi = 1$, the standard cosmological scenario, to $\xi = 500, 1000$ cases makes it clear that freeze-out during an early cosmological period of QCD confinement, which can realize the observed relic density for weaker couplings, can make the difference between a freeze-out relic WIMP being allowed versus strongly excluded by direct searches.

There are a number of features in Figure 4.4 that warrant further discussion:

- The $\xi \gg 1$ lines end when $m_\chi^{T=T_F} \sim \Lambda_{\rm QCD} \equiv \xi \Lambda_{\rm QCD}^{\rm SM}$, at which point the dark matter mass is heavier than the QCD scale, and the resulting annihilation would be into quarks and not into pions.

- For standard cosmology, with $\xi = 1$, the kink in the annihilation cross section at $m_\chi \sim 173$ GeV corresponds to the annihilation channel into top quarks opening up. Similarly, the kinks in the $\xi = 500, 1000$ lines correspond to new channels into heavier

[1] Our choice of couplings β_{ij} aligned with the Yukawa interactions leads to diagonal interactions between the dark matter and the pion mass eigenstates.

pions.

- As mentioned earlier, the annihilation cross section is enhanced by the QCD scale. Therefore this scenario accommodates larger values of the mediator scale, $M_S \sim 10^6$ GeV, compared to a standard WIMP scenario.

- The effect of the quark-condensate contribution to the dark matter mass can be seen in the bottom-right panel. Depending on the sign of β in 4.21, there are two values of $m_\chi^{T=T_F}$ which correspond to a single $m_\chi^{T=0}$ for modest dark matter masses.

- The bottom left panel implies that a scenario in which the QCD deconfinement brings the dark matter back into equilibrium with quarks after it has frozen out from interacting with mesons is never realized, for deconfinement happening below a few GeV.

4.4.4 Vector-Mediator Results

For vector interactions, our choice of minimally flavor-violating interactions λ_{ij} with the quarks results in leading interactions with a pair of pions, as in Equation (4.20). In the non-relativistic limit, the thermally-averaged annihilation cross section is,

$$\langle \sigma_V v \rangle = \sum_{a,b=1}^{35} \frac{\Omega_{ab}}{24\pi} m_\chi^2 (1 - \gamma_{ab} + \rho_{ab})^{3/2} \left[1 + \left(1 + \frac{9}{4} \frac{\gamma_{ab} - 2\rho_{ab}}{1 - \gamma_{ab} + \rho_{ab}} \right) \frac{\langle v^2 \rangle}{2} + \mathcal{O}(\langle v^4 \rangle) \right] \quad (4.30)$$

summed over pairs of mesons for which $m_{\pi_a} + m_{\pi_b} \leq 2m_\chi$. Note that vector interactions do not induce a shift in the mass of the dark matter from the chiral condensate. The coupling matrix Ω_{ab} is given by

$$\Omega_{ab} \equiv \sum_{c,d=1}^{35} \frac{1}{M_V^4} f^{abc} \, \mathrm{tr}[T^c \lambda] \, f^{abd} \, \mathrm{tr}[T^d \lambda] \propto \frac{\alpha^2}{M_V^4} \ , \quad (4.31)$$

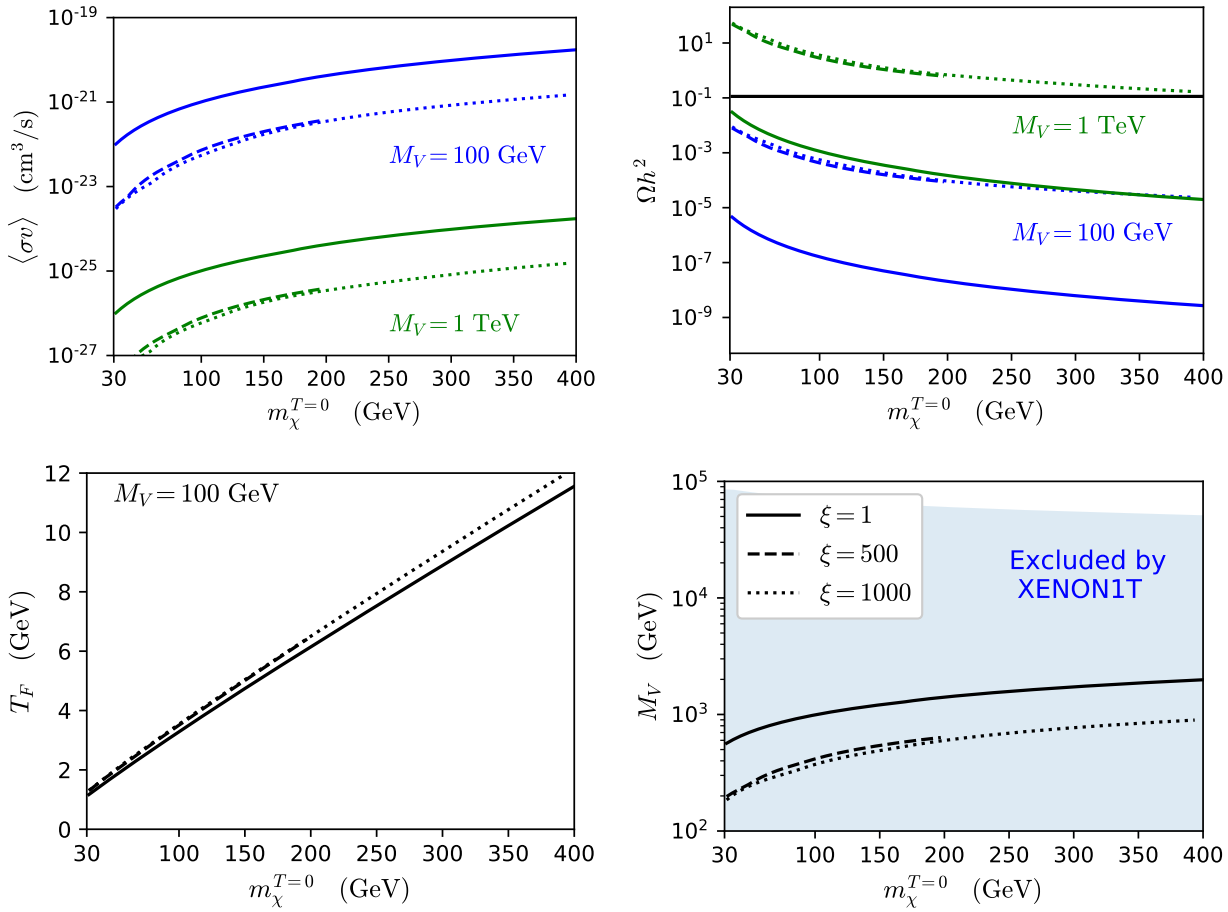

Figure 4.5: **(Top Left)** The thermally-averaged cross-sections at the time of freeze-out as a function of $m_\chi^{T=0}$ plotted for $M_V = 100$ GeV (blue), 1 TeV (green) and ξ =1 (solid), 500 (dashed), 1000 (dotted). **(Top Right)** The generated relic abundance today as a function of $m_\chi^{T=0}$ plotted for $M_V = 100$ GeV (blue), 1 TeV (green) and ξ =1 (solid), 500 (dashed), 1000 (dotted). The horizontal solid line is the observed dark matter abundance. **(Bottom Left)** The freeze-out temperature as a function of $m_\chi^{T=0}$ with $M_V = 100$ GeV plotted for ξ =1 (solid), 500 (dashed), 1000 (dotted). **(Bottom Right)** Coupling as a function of $m_\chi^{T=0}$ to produce the observed relic density plotted for ξ =1 (solid), 500 (dashed), 1000 (dotted). Shaded blue region is excluded by XENON1T. See text for details.

where we focus on $\alpha = 1$ for simplicity. The kinematic factors are defined as $\gamma_{ab} \equiv (m_{\pi_a}^2 + m_{\pi_b}^2)/(2m_\chi^2)$ and $\rho_{ab} \equiv (m_{\pi_a}^2 - m_{\pi_b}^2)^2/(16m_\chi^4)$.

In Figure 4.5 we show the resulting annihilation cross section, relic density, and freeze-out temperature, as a function of the dark matter mass at zero temperature $m_\chi^{T=0}$, for two choices of $M_V = 100$ GeV, 1 TeV and $\xi = 1, 500, 1000$, where $\xi = 1$ corresponds to the standard

picture of freeze-out through annihilation into quarks. In the final panel, we show the value of M_V for each dark matter mass required to reproduce the observed relic density for a given choice of ξ.

Unlike the scalar interactions, vector interactions do not get the $\xi-$enhancement from QCD confinement. On the contrary the annihilation cross-section is smaller than the standard WIMP scenario because the annihilation products, namely the new pions, are heavier than SM quarks at the same temperature in standard cosmology. Hence, the vector scenario does worse than the standard WIMP case within this cosmological history.

4.5 Conclusions

The standard picture of freeze out is a compelling picture for the mechanism by which dark matter is produced in the early Universe, and the primary motivation for WIMP dark matter. Common wisdom states that the WIMP paradigm is in trouble, but this is the result of comparing freeze out in a standard cosmology to searches for WIMPs. In this article, we have explored the possibility that the cosmology looks radically different at the time of freeze out, in particular exploring the idea that QCD could have undergone an early period of confinement before relaxing to the behavior observed at low temperatures today. We find that for a scalar mediator, the dark matter mass is shifted by the chiral condensate, and its coupling to pions is enhanced during early confinement, allowing for parameter space which allows for freeze out production while remaining safe from constraints from XENON1T today, rescuing some of the WIMP parameter space. On the other hand, for a vector mediator we find that the differences between freeze out during early confinement and the standard cosmology are more modest, and the entire parameter space remains ruled out by XENON1T. Our work highlights the fact that a modified cosmology may largely distort the apparent messages from astrophysical observations of dark matter to inform particle

physics model building.

Chapter 5

Conclusions

In this dissertation, we have considered dark matter which communicates to the Standard Model via coupling directly to the quarks. In Chapter 2 we considered a vector-like coupling of the form $\alpha_q v_\mu(\overline{q}\gamma^\mu q)$, and in Chapter 3 we considered a an axial-vector coupling of the form $\alpha_q a_\mu(\overline{q}\gamma^\mu\gamma^5 q)$.

In Chapters 2 and 3 we have argued the set of all possible mesonic final states resulting from DM annihilation/decay from kinematics and symmetry considerations. Moreover, we have also found the set of all final states by way of the chiral Lagrangian description of the DM-quark coupling at energies below the confinement scale, which is in agreement with our arguments from symmetry. From these final states we then found the photon spectrum for dark matter annihilation and compared this to current observations of the diffuse emission and prospective future searches in the Draco galaxy. We found that current observations of the diffuse photon background emission can already be used to obtain an upper bound on the total dark matter annihilation cross section in a Lagrangian-free manner, as well as the model parameters themselves when using the chiral Lagrangian description. Furthermore, we have found that future observations of dwarf spheroidal galaxies (dSphs) will significantly refine

the bounds on the models' parameter space or possibly discover this model, as it provides a lower bound on the total dark matter annihilation cross section.

In Chapter 4 we have explored a non-standard cosmology that looks drastically different at the time of dark matter freeze out. In particular, we explored the idea that QCD could have undergone an early period of confinement before relaxing to the behavior observed at low temperatures today. We find that for a scalar dark matter mediator, the dark matter mass is shifted by the chiral condensate and its coupling to pions is enhanced during early confinement. This enhancement admits a parameter space which allows for freeze out production while remaining safe from constraints from XENON1T today, rescuing some of the WIMP parameter space from being excluded by direct detection experiments. On the other hand, for a vector dark matter mediator we find that the differences between freeze out during early confinement and the standard cosmology are more modest, and the entire parameter space remains ruled out by XENON1T direct detection searches.

Bibliography

[1] A. De Angelis et al. Science with e-ASTROGAM: A space mission for MeV–GeV gamma-ray astrophysics. *Journal of High Energy Astrophysics*, 19:1–106, 2017.

[2] R. Caputo, M. Meyer, and M. Sanchez-conde. AMEGO: Dark Matter Prospects. 2017.

[3] S. Hunter and J. Buckley. The Advanced Pair Telescope (APT) Mission Concept. 2008.

[4] K. Boddy and J. Kumar. Indirect Detection of Dark Matter Using MeV-Range Gamma-Ray Telescopes. *Physical Review D*, 92:023533, 2015.

[5] K. Boddy and J. Kumar. Minding the MeV Gap: the Indirect Detection of Low Mass Dark Matter. *arXiv: Cosmology and Nongalactic Astrophysics*, 2015.

[6] K. Boddy, K. Dienes, Doojin Kim, J. Kumar, Jong-Chul Park, and B. Thomas. Lines and boxes: Unmasking Dynamical Dark Matter through correlations in the MeV gamma-ray spectrum. *Physical Review D*, 94:095027, 2016.

[7] R. Bartels, D. Gaggero, and C. Weniger. Prospects for indirect dark matter searches with MeV photons. *Journal of Cosmology and Astroparticle Physics*, 2017:001–001, 2017.

[8] O. Catà, A. Ibarra, and Sebastian Ingenhutt. Sharp spectral features from light dark matter decay via gravity portals. *arXiv: High Energy Physics - Phenomenology*, 2017.

[9] Maíra Dutra, M. Lindner, S. Profumo, F. Queiroz, W. Rodejohann, and C. Siqueira. MeV Dark Matter Complementarity and the Dark Photon Portal. *arXiv: High Energy Physics - Phenomenology*, 2018.

[10] J. Kumar. Indirect detection of sub-GeV dark matter coupling to quarks. *Physical Review D*, 98, 2018.

[11] Debajyoti Choudhury and Divya Sachdeva. Model independent analysis of MeV scale dark matter: Cosmological constraints. *Phys. Rev. D*, 100:035007, Aug 2019.

[12] J. Gasser and H. Leutwyler. Chiral Perturbation Theory: Expansions in the Mass of the Strange Quark. *Nuclear Physics*, 250:465–516, 1985.

[13] J. Gasser and H. Leutwyler. Chiral perturbation theory to one loop. *Annals of Physics*, 158:142–210, 1984.

[14] U. Meißner. Recent developments in chiral perturbation theory. *Reports on Progress in Physics*, 56:903–996, 1993.

[15] G. Ecker. Chiral perturbation theory. *Progress in Particle and Nuclear Physics*, 35:1–80, 1995.

[16] G. Colangelo and G. Isidori. An Introduction to ChPT. 2000.

[17] S. Scherer. Introduction to Chiral Perturbation Theory. *Advances in Nuclear Physics*, 27:277–538, 2002.

[18] C. Terschlüsen, S. Leupold, and M. Lutz. Electromagnetic transitions in an effective chiral lagrangian with the η' and light vector mesons. *The European Physical Journal A*, 48:1–17, 2012.

[19] C. Terschlusen and S. Leupold. Renormalization of the low-energy constants of chiral perturbation theory from loops with dynamical vector mesons. *Physical Review D*, 94:014021, 2016.

[20] M. Tanabashi et al. Review of Particle Physics. *Phys. Rev. D*, 98:030001, Aug 2018.

[21] A. Strong, I. Moskalenko, and O. Reimer. Diffuse Galactic continuum gamma rays. A model compatible with EGRET data and cosmic-ray measurements. *The Astrophysical Journal*, 613:962–976, 2004.

[22] A. Geringer-Sameth and S. Koushiappas. Exclusion of canonical WIMPs by the joint analysis of Milky Way dwarfs with Fermi. 2011.

[23] M. N. Mazziotta, F. Loparco, F. Palma, and N. Giglietto. A model-independent analysis of the Fermi Large Area Telescope gamma-ray data from the Milky Way dwarf galaxies and halo to constrain dark matter scenarios. *Astroparticle Physics*, 37:26–39, 2012.

[24] A. Geringer-Sameth, S. Koushiappas, and M. Walker. Comprehensive search for dark matter annihilation in dwarf galaxies. *Physical Review D*, 91:083535, 2015.

[25] K. Boddy, J. Kumar, D. Marfatia, and Pearl Sandick. Model-independent constraints on dark matter annihilation in dwarf spheroidal galaxies. *Physical Review D*, 97:095031, 2018.

[26] A. Albert et al. Dark Matter Limits from Dwarf Spheroidal Galaxies with the HAWC Gamma-Ray Observatory. *The Astrophysical Journal*, 853:154, 2017.

[27] M. Cirelli, G. Corcella, A. Hektor, G. Hutsi, M. Kadastik, P. Panci, M. Raidal, F. Sala, and A. Strumia. PPPC 4 DM ID: a poor particle physicist cookbook for dark matter indirect detection. *Journal of Cosmology and Astroparticle Physics*, 2011:051–051, 2012.

[28] A. Geringer-Sameth, S. Koushiappas, and M. Walker. Dwarf galaxy annihilation and decay emission profiles for dark matter experiments. *arXiv: Cosmology and Nongalactic Astrophysics*, 2014.

[29] N. Aghanim et al. (Planck Collaboration). Planck 2018 results. VI. Cosmological parameters. *Astronomy and Astrophysics*, 641:1–67, 2020.

[30] T. Slatyer. Energy injection and absorption in the cosmic dark ages. *Physical Review D*, 87:123513, 2013.

[31] H. Kluck et al. (CRESST Collaboration). Search for low-mass Dark Matter with the CRESST Experiment. *arXiv: Instrumentation and Methods for Astrophysics*, 2017.

[32] Spencer Chang, Jia Liu, A. Pierce, N. Weiner, and I. Yavin. CoGeNT Interpretations. 2010.

[33] Jonathan L. Feng, J. Kumar, D. Marfatia, and D. Sanford. Isospin-violating dark matter. *Physics Letters B*, 703:124–127, 2011.

[34] Jonathan L. Feng, J. Kumar, and D. Sanford. Xenophobic dark matter. *Physical Review D*, 88:015021, 2013.

[35] J. Kumar and D. Marfatia. Matrix element analyses of dark matter scattering and annihilation. *Physical Review D*, 88:014035, 2013.

[36] P. Adlarson et al. Measurement of the $\omega \to \pi^+\pi^-\pi^0$ Dalitz plot distribution. *Phys. Lett. B*, 770:418–425, 2017.

[37] K. Boddy, K. Dienes, Doojin Kim, J. Kumar, Jong-Chul Park, and B. Thomas. Boxes, boosts, and energy duality: Understanding the Galactic Center gamma-ray excess through Dynamical Dark Matter. *Physical Review D*, 95:055024, 2016.

[38] J.H. Buckley. private communications.

[39] Amego collaboration website. `https://asd.gsfc.nasa.gov/amego/technical.html`.

[40] S. Jiang et al. Computation of the p^6 order chiral Lagrangian coefficients. *Phys. Rev. D*, 81:014001, 2010.

[41] G. Blumenthal, S. Faber, J. Primack, and M. Rees. Formation of galaxies and large-scale structure with cold dark matter. *Nature*, 311:517–525, 1984.

[42] Dillon Berger, A. Rajaraman, and J. Kumar. Dark matter through the quark vector current portal. *Pramana*, 94:1–11, 2019.

[43] L. Strigari, S. Koushiappas, J. Bullock, M. Kaplinghat, J. Simon, M. Geha, and B. Willman. The most dark-matter-dominated galaxies : Predicted gamma-ray signals from the faintest milky way dwarfs. *The Astrophysical Journal*, 678:614–620, 2008.

[44] M. Odenkirchen et al. Detection of massive tidal tails around the globular cluster palomar 5 with sloan digital sky survey commissioning data. *The Astrophysical Journal*, 548(2):L165–L169, feb 2001.

[45] J. Kleyna, M. Wilkinson, N. Evans, and G. Gilmore. Dark matter in dwarf spheroidals – ii. observations and modelling of draco. *Monthly Notices of the Royal Astronomical Society*, 330:792–806, 2002.

[46] E. L. Lokas. Dark matter distribution in dwarf spheroidal galaxies. *Monthly Notices of the Royal Astronomical Society*, 333:697–708, 2002.

[47] R. Klessen, E. Grebel, D. H. A. I. Potsdam, U. Cruz, M. F. Astronomie, and Heidelberg. Draco: A failure of the tidal model. *The Astrophysical Journal*, 589:798–809, 2003.

[48] Seyda Ipek and Tim M. P. Tait. Early Cosmological Period of QCD Confinement. *Phys. Rev. Lett.*, 122(11):112001, 2019.

[49] Djuna Croon, Jessica N. Howard, Seyda Ipek, and Timothy M. P. Tait. QCD Baryogenesis. 2019.

[50] E. Aprile et al. Dark Matter Search Results from a One Ton-Year Exposure of XENON1T. *Phys. Rev. Lett.*, 121(11):111302, 2018.

[51] G. Hinshaw et al. Nine-Year Wilkinson Microwave Anisotropy Probe (WMAP) Observations: Cosmological Parameter Results. *Astrophys. J. Suppl.*, 208:19, 2013.

[52] M. L. Ahnen et al. Limits to Dark Matter Annihilation Cross-Section from a Combined Analysis of MAGIC and Fermi-LAT Observations of Dwarf Satellite Galaxies. *JCAP*, 1602:039, 2016.

[53] Maria Beltran, Dan Hooper, Edward W. Kolb, and Zosia C. Krusberg. Deducing the nature of dark matter from direct and indirect detection experiments in the absence of collider signatures of new physics. *Phys. Rev.*, D80:043509, 2009.

[54] Morad Aaboud et al. Search for dark matter and other new phenomena in events with an energetic jet and large missing transverse momentum using the ATLAS detector. *JHEP*, 01:126, 2018.

[55] Albert M Sirunyan et al. Search for dark matter produced with an energetic jet or a hadronically decaying W or Z boson at $\sqrt{s} = 13$ TeV. *JHEP*, 07:014, 2017.

[56] Jonathan L. Feng and Jason Kumar. The WIMPless Miracle: Dark-Matter Particles without Weak-Scale Masses or Weak Interactions. *Phys. Rev. Lett.*, 101:231301, 2008.

[57] Marat Freytsis and Zoltan Ligeti. On dark matter models with uniquely spin-dependent detection possibilities. *Phys. Rev.*, D83:115009, 2011.

[58] Jessica Goodman, Masahiro Ibe, Arvind Rajaraman, William Shepherd, Tim M. P. Tait, and Hai-Bo Yu. Constraints on Dark Matter from Colliders. *Phys. Rev.*, D82:116010, 2010.

[59] Seyda Ipek, David McKeen, and Ann E. Nelson. A Renormalizable Model for the Galactic Center Gamma Ray Excess from Dark Matter Annihilation. *Phys. Rev.*, D90(5):055021, 2014.

[60] Mohammad Abdullah, Anthony DiFranzo, Arvind Rajaraman, Tim M. P. Tait, Philip Tanedo, and Alexander M. Wijangco. Hidden on-shell mediators for the Galactic Center γ-ray excess. *Phys. Rev.*, D90:035004, 2014.

[61] David Tucker-Smith and Neal Weiner. Inelastic dark matter. *Phys. Rev.*, D64:043502, 2001.

[62] Céline Boehm, Matthew J. Dolan, Christopher McCabe, Michael Spannowsky, and Chris J. Wallace. Extended gamma-ray emission from Coy Dark Matter. *JCAP*, 1405:009, 2014.

[63] Marco Cirelli, Nicolao Fornengo, and Alessandro Strumia. Minimal dark matter. *Nucl. Phys.*, B753:178–194, 2006.

[64] Graciela B. Gelmini and Paolo Gondolo. Neutralino with the right cold dark matter abundance in (almost) any supersymmetric model. *Phys. Rev.*, D74:023510, 2006.

[65] Saleh Hamdan and James Unwin. Dark Matter Freeze-out During Matter Domination. *Mod. Phys. Lett.*, A33(29):1850181, 2018.

[66] G. D'Ambrosio, G. F. Giudice, G. Isidori, and A. Strumia. Minimal flavor violation: An Effective field theory approach. *Nucl. Phys.*, B645:155–187, 2002.

[67] Yang Bai and Tim M. P. Tait. Inelastic Dark Matter at the LHC. *Phys. Lett.*, B710:335–338, 2012.

[68] Edward W. Kolb and Michael S. Turner. The Early Universe. *Front. Phys.*, 69:1–547, 1990.

[69] Richard J. Hill and Mikhail P. Solon. Standard Model anatomy of WIMP dark matter direct detection II: QCD analysis and hadronic matrix elements. *Phys. Rev.*, D91:043505, 2015.

[70] Kirtimaan A. Mohan, Dipan Sengupta, Tim M. P. Tait, Bin Yan, and C. P. Yuan. Direct Detection and LHC constraints on a t-Channel Simplified Model of Majorana Dark Matter at One Loop. *JHEP*, 05:115, 2019.

[71] Mikhail A. Shifman, A. I. Vainshtein, and Valentin I. Zakharov. Remarks on Higgs Boson Interactions with Nucleons. *Phys. Lett.*, 78B:443–446, 1978.

[72] S. Troitsky. Unsolved problems in particle physics. *Physics-Uspekhi*, 55:72–95, 2012.

[73] M. Schumann, L. Baudis, L. Butikofer, A. Kish, and M. Selvi. Dark matter sensitivity of multi-ton liquid xenon detectors. *arXiv: Instrumentation and Detectors*, 2015.

[74] Dillon Berger, Seyda Ipek, T. Tait, and M. Waterbury. Dark Matter Freeze Out during an Early Cosmological Period of QCD Confinement. *arXiv: High Energy Physics - Phenomenology*, 2020.

Appendix A

The Vector Portal Appendix

A.1 Symmetry considerations

Since we assume that the primary dark matter annihilation/decay process does not involve weak interactions, we will find that the hadronic final state has vanishing strangeness, and has the same parity, charge conjugation and angular momentum quantum numbers as the initial state. We also, for simplicity, focus only on primary annihilation/decay processes which produce at most two mesons. As such, the only kinematically accessible neutral two-body final states with vanishing net strangeness are $\pi\pi$, $\eta\eta$, $\eta\pi^0$, $\rho\pi$, $\omega\pi^0$, K^+K^-, $K^0\bar{K}^0$.

The quantum numbers of the Standard Model final state can be determined in general from the quantum numbers of the dark matter initial state (for example, see [35]). If dark matter couples to a vector quark current, the final state necessarily has $J^{PC} = 1^{--}$. As such, the $\pi^0\pi^0$, $\eta\pi^0$, $\eta\eta$, K_LK_L and K_SK_S final states are forbidden. As a result, the only final states which we need consider are $\pi^+\pi^-$, K^+K^-, K^LK^S, $\rho\pi$, and $\omega\pi^0$. Since all of the mesons in question have odd intrinsic parity, each state transforms under parity as $(-1)^L$, and must thus have orbital angular momentum $L = odd$. From the symmetry of the wavefunction, we

then see that the $\pi^+\pi^-$ state must have isospin $I = 1$, $I_3 = 0$. Similarly, we can classify the two-kaon final states in terms of their isospin quantum numbers:

$$\begin{aligned}(KK)_s &= \frac{1}{\sqrt{2}}\left(|K^+K^-\rangle + |K_LK_S\rangle\right) \qquad I = 0, \\ (KK)_t &= \frac{1}{\sqrt{2}}\left(|K^+K^-\rangle - |K_LK_S\rangle\right) \qquad I = 1,\ I_3 = 0. \end{aligned} \tag{A.1}$$

Note, the choice of which relative sign corresponds to the singlet or triplet state is a convention, which depends on the normalizations of the $|K^+K^-\rangle$ and $|K_LK_S\rangle$ states. The $\omega\pi^0$ state is necessarily $I = 1$, $I_3 = 0$, while the $\rho\pi$ state is $I = 0, 1$ or 2, $I_3 = 0$. But since the isospin quantum numbers of the final state should be the same as those of the quark current to which the vector spurion couples, we should only be only be able to produce $\rho\pi$ states with $I = 0$ or 1; the $I = 2$ $\rho\pi$ state should be inaccessible.

Thus, we essentially have six final states, two of which have $I = I_3 = 0$ ($(KK)_s$ and $(\rho\pi)_s$), and four of which have $I = 1$, $I_3 = 0$ ($(\pi\pi)_t$, $(KK)_t$, $(\rho\pi)_t$ and $(\omega\pi)_t$). Note that the $(\pi\pi)_t$ state produces no photons, while the $(KK)_s$ and $(KK)_t$ states produce identical photon spectra.

Isospin is an $SU(2)$ subgroup of the QCD flavor symmetries which relates u- and d-quarks. But similarly, there are $SU(2)$ subgroups which related d- and s-quarks (U-spin) and u- and s-quarks (V-spin). We thus find that the K^+K^- state must have V-spin $I^V = 1$, $I_3^V = 0$, while the states $(1/\sqrt{2})(|\pi^+\pi^-\rangle \pm |K_LK_S\rangle)$ have $I^V = I_3^V = 0$ and $I^V = 1$, $I_3^V = 0$, respectively. Similarly, the K^LK^S state must have U-spin $I^U = 1$, $I_3^U = 0$, while the states $(1/\sqrt{2})(|\pi^+\pi^-\rangle \pm |K^+K^-\rangle)$ have $I^U = I_3^U = 0$ and $I^U = 1$, $I_3^U = 0$, respectively. Note that U-spin and V-spin are not useful for classifying the $\rho\pi$ and $\omega\pi^0$ final states, since the ρ and ω transform into kinematically inaccessible states under U-spin and V-spin; essentially, the ρ and ω are necessarily close enough to threshold that the strange quark mass cannot be

taken as negligible.

A.2 Feynman Rules: Vector Portal Dark Matterl

We here collect the relevant Feynman rules. For all rules below, all momenta on the left are entering the vertex, and those on the right are exiting.

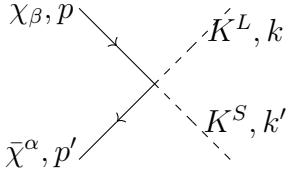

$$\frac{1}{\Lambda^2}(\gamma^\mu)_\alpha{}^\beta(\alpha_d - \alpha_s)(k-k')_\mu$$

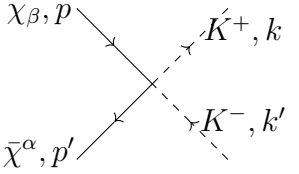

$$\frac{1}{\Lambda^2}(\gamma^\mu)_\alpha{}^\beta(\alpha_d - \alpha_s)(k-k')_\mu \tag{A.2}$$

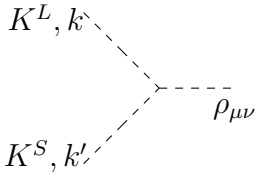

$$i\frac{4f_V h_P}{F^2}(k^\mu(k')^\nu - k^\nu(k')^\mu)$$

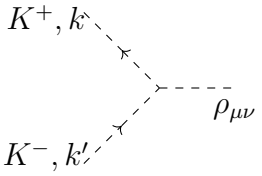

$$i\frac{4f_V h_P}{F^2}(k^\mu(k')^\nu - k^\nu(k')^\mu) \tag{A.3}$$

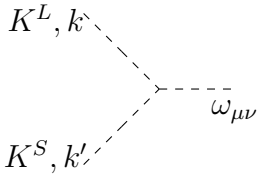

$$-i\frac{4f_V h_P}{F^2}(k^\mu (k')^\nu - k^\nu (k')^\mu)$$

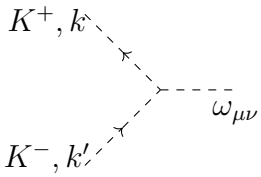

$$-i\frac{4f_V h_P}{F^2}(k^\mu (k')^\nu - k^\nu (k')^\mu) \tag{A.4}$$

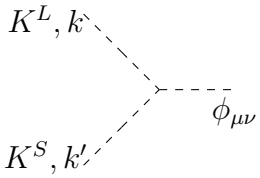

$$i\sqrt{2}\frac{4f_V h_P}{F^2}(k^\mu (k')^\nu - k^\nu (k')^\mu)$$

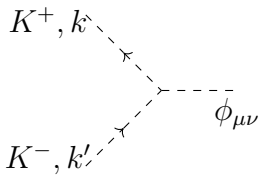

$$i\sqrt{2}\frac{4f_V h_P}{F^2}(k^\mu (k')^\nu - k^\nu (k')^\mu) \tag{A.5}$$

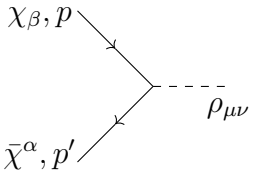

$$-\frac{f_V}{2\Lambda^2}\Big(i(p+p')_\nu \gamma^\mu - i(p+p')_\mu \gamma^\nu\Big)(\alpha_d - \alpha_u) \tag{A.6}$$

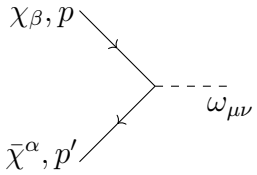

$$\frac{f_V}{2\Lambda^2}\Big(i(p+p')_\nu\gamma^\mu - i(p+p')_\mu\gamma^\nu\Big)(\alpha_d+\alpha_u) \tag{A.7}$$

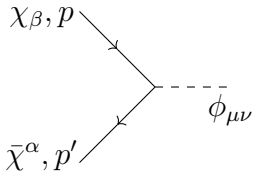

$$\sqrt{2}\frac{f_V}{2\Lambda^2}\Big(i(p+p')_\nu\gamma^\mu - i(p+p')_\mu\gamma^\nu\Big)\alpha_s \tag{A.8}$$

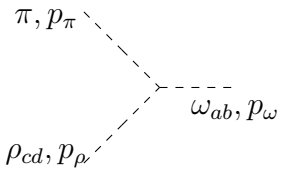

$$\begin{aligned}\frac{1}{2\sqrt{F}}\Big(&2h_A\varepsilon^{cdbh}(p_\pi)_h(p_\omega)^a + 2h_A\varepsilon^{abdh}(p_\pi)_h(p_\rho)^c \\ &+h_O\varepsilon^{cdgb}(p_\rho)_g(p_\pi)^a + h_O\varepsilon^{abgd}(p_\omega)_g(p_\pi)^c\Big)\end{aligned} \tag{A.9}$$

A.3 Decay Spectra at Rest

We begin by finding the decay spectrum at rest for the various mesons. For two-body decays the spectra are set by kinematics. For a decay $A \to B + C$ the energy spectrum of B is

$$\frac{d\Gamma}{dE_B} = \delta\left(E_B - \frac{m_B^2 + m_A^2 - m_C^2}{2m_A}\right). \tag{A.10}$$

Three body decays must be analyzed in terms of Dalitz plots, which encode the amplitudes as a function of the kinematic variables.

$K^+(p_K) \to \bar{\ell}(p_1)\nu(p_2)\pi^0(p_3)$

The decay to $K^+(p_K) \to \bar{\ell}(p_1)\nu(p_2)\pi^0(p_3)$ is controlled by the matrix element $\mathcal{M} = (p_K + p_3)^\mu \bar{\ell}\gamma_\mu(1-\gamma_5)\nu$. The pion energy spectrum is controlled by

$$\Gamma = \int dm_{12}^2 dm_{23}^2 \sum_{spins} |\mathcal{M}|^2. \tag{A.11}$$

We then find that

$$\begin{aligned}\frac{d\Gamma}{dm_{12}^2} \propto \int dm_{23}^2\ |\mathcal{M}|^2 \quad \propto \quad & -8m_\ell^2(m_\pi^2 + m_\ell^2 - m_{12}^2) - 8m_K^2 m_\pi^2((m_{23}^2)_{max} - (m_{23}^2)_{min}) \\ & +4(m_K^2 + 2m_\ell^2 + m_\pi^2 - m_{12}^2)((m_{23}^4)_{max} - (m_{23}^4)_{min}) \\ & -\frac{8}{3}((m_{23}^6)_{max} - (m_{23}^6)_{min}),\end{aligned} \tag{A.12}$$

where we have defined

$$E_2^* = \frac{m_{12}^2 - m_1^2 + m_2^2}{2m_{12}} \qquad E_3^* = \frac{M^2 - m_{12}^2 - m_3^2}{2m_{12}},$$
$$m_{ij}^2 = (p_i - p_j)^2\,,$$
$$(m_{23}^2)_{max} = (E_2^* + E_3^*)^2 - \left(\sqrt{(E_2^*)^2 - m_2^2} - \sqrt{(E_3^*)^2 - m_3^2}\right)^2,$$
$$(m_{23}^2)_{min} = (E_2^* + E_3^*)^2 - \left(\sqrt{(E_2^*)^2 - m_2^2} + \sqrt{(E_3^*)^2 - m_3^2}\right)^2. \tag{A.13}$$

$K^+(p_K) \to \pi^0(p_1)\pi^0(p_2)\pi^+(p_3)$

The decay $K^+(p_K) \to \pi^0(p_1)\pi^0(p_2)\pi^+(p_3)$ can be expressed in terms of the invariant amplitude $\mathcal{A}$ [20]

$$\begin{aligned} |\mathcal{A}|^2 &= \frac{d\Gamma}{ds_3 ds_2} \propto 1 + g\frac{(s_3 - s_0)}{m_+^2} + h\left(\frac{(s_3 - s_0)}{m_+^2}\right)^2 + k\left(\frac{s_2 - s_1}{m_+^2}\right)^2, \\ &= 1 + g\frac{(s_3 - s_0)}{m_+^2} + h\left(\frac{(s_3 - s_0)}{m_+^2}\right)^2 + k\left(\frac{2s_2 + s_3 - 3s_0}{m_+^2}\right)^2, \end{aligned} \tag{A.14}$$

where

$$s_i = (p_K - p_i)^2 \qquad s_0 = \frac{s_1 + s_2 + s_3}{3} = \frac{1}{3}(m_K^2 + m_1^2 + m_2^2 + m_3^2),$$
$$g = 0.626 \qquad h = 0.052 \qquad k = 0.0054. \tag{A.15}$$

The pion energy distribution is then

$$\frac{d\Gamma}{dE_2} = -2m_K \frac{d\Gamma}{ds_2} \propto \int ds_3 \; |\mathcal{A}|^2. \tag{A.16}$$

We then find that the energy distribution of π_0 in decays of $K^+ \to \pi^0\pi^0\pi^+$ at rest is (here E_2 is the neutral pion energy)

$$\frac{d\Gamma}{dE_2} \;\; = \;\; \mathcal{N}_{K^+\to\pi^+\pi^0\pi^0}\sigma(s_2)\left(\alpha_0 + +\alpha s_2 + \frac{\alpha_1}{s_2} + \frac{\alpha_2}{s_2^2} + \frac{\alpha_3}{s_3^3}\right), \tag{A.17}$$

where

$$\sigma(s_2) = \frac{\sqrt{\left[-2m_+^2\left(m_\pi^2+s_2\right)+\left(m_\pi^2-s_2\right)^2+m_+^4\right]\left[-2m_\pi^2\left(m_{K_+}^2+s_2\right)+\left(m_{K_+}^2-s_2\right)^2+m_\pi^4\right]}}{2m_+^2} \tag{A.18}$$

and

$$\begin{cases} \alpha_0 = -g - \frac{2}{3}h\left(1+\frac{m_{K_+}^2+2m_\pi^2}{m_+^2}\right), \\ \alpha = \frac{2}{3m_+^2}h, \\ \alpha_1 = 2m_+^2 + \frac{g}{3}\left(m_{K_+}^2+m_+^2+2m_\pi^2\right) + \frac{h}{9}\left(\frac{20m_\pi^4+2m_{K_+}^4-4m_\pi^2m_{K_+}^2}{m_+^2}+16m_{K_+}^2-4m_\pi^2+2m_+^2\right), \\ \alpha_2 = g\left(m_\pi^2m_{K_+}^2-m_+^2m_{K_+}^2-m_\pi^4+m_+^2m_\pi^2\right)+\frac{2}{3}h\left(\frac{m_\pi^4m_{K_+}^2-2m_\pi^6}{m_+^2}+2m_\pi^2m_{K_+}^2-m_+^2m_{K_+}^2-m_{K_+}^4+m_\pi^4\right), \\ \alpha_3 = 2h\frac{\left(m_+^2-m_\pi^2\right)^2\left(m_\pi^2-m_{K_+}^2\right)^2}{3m_+^2}. \end{cases} \tag{A}$$

We find that the normalization constant by integrating both sides with respect to dE (picking up a factor of $-\frac{1}{2m_{K_+}}$). The normalization constant is given by,

$$\mathcal{N}_{K^+\to\pi^+\pi^0\pi^0} = -0.00187217 \text{ (GeV)}^3.$$

$K_L(p_K) \to \pi^+(p_1)\pi^-(p_2)\pi^0(p_3), \pi^0(p_1)\pi^0(p_2)\pi^0(p_3)$

The decay $K_L(p_K) \to \pi^+(p_1)\pi^-(p_2)\pi^0(p_3)$ can be expressed in terms of the invariant amplitude $\mathcal{A}$ [20]

$$|\mathcal{A}(s_1,s_2,s_3)|^2 = 1 + g\frac{(s_3-s_0)}{m_{\pi^+}^2} + h\left(\frac{s_3-s_0}{m_{\pi^+}^2}\right)^2 + j\frac{(s_2-s_1)}{m_{\pi^+}^2} + k\left(\frac{s_2-s_1}{m_{\pi^+}^2}\right)^2 + f\frac{(s_2-s_1)}{m_{\pi^+}^2}\frac{(s_3-s_0)}{m_{\pi^+}^2} + (\text{A.2}$$

Here

$$s_i = (p_K - p_i)^2 \qquad s_0 = \frac{s_1+s_2+s_3}{3} = \frac{1}{3}(m_K^2 + m_1^2 + m_2^2 + m_3^2),$$
$$g = 0.678 \qquad h = 0.076 \qquad j = 0.001 \qquad f = 0.0045 \qquad k = 0.0099. \tag{A.21}$$

The pion energy distribution is then (here E_3 is the neutral pion energy)

$$\frac{d\Gamma}{dE_3} \propto \int ds_2 \; |\mathcal{A}|^2 \tag{A.22}$$

We then find that the energy distribution of π_0 in decays of $K_L \to \pi^+\pi^-\pi^0$ at rest is proportional to

$$\begin{aligned}\frac{d\Gamma}{dE_3} &= \left[1 + g\frac{(s_3 - s_0)}{m_\pi^2} + h(\frac{(s_3 - s_0)}{m_\pi^2})^2 + (j + f\frac{(s_3 - s_0)}{m_\pi^2})\frac{(-3s_0 - s_3)}{m_\pi^2} + k(\frac{(-3s_0 - s_3)}{m_\pi^2})^2\right]\sigma \\ &+ \left(j + f\frac{(s_3 - s_0)}{m_\pi^2} + 2k\frac{(-3s_0 - s_3)}{m_\pi^2}\right)\sigma(3s_0 - s) \\ &+ \frac{4}{3}k\frac{1}{m_\pi^4}\sigma\left(\frac{3}{4}(3s_0 - s)^2 + \frac{1}{4}\sigma^2\right), \end{aligned} \tag{A.23}$$

where

$$\sigma = \sqrt{1 - \frac{4M_\pi^2}{s}}\left(s - (M_K + M_\pi)^2\right)^{1/2}\left(s - (M_K - M_\pi)^2\right)^{1/2}. \tag{A.24}$$

For the $K_L \to 3\pi^0$ decay, we have [20]

$$|\mathcal{A}|^2 = 1 + h\frac{(s_3 - s_0)^2}{m_+^4}, \tag{A.25}$$

where $h = 0.59$. The energy distribution may then be found similarly to the calculation for $K_L \to \pi^+\pi^-\pi^0$ above.

$\omega \to \pi^0(p_1)\pi^+(p_2)\pi^-(p_3)$

ω decays to three pions are described by a similar Dalitz plot, which was taken from [36].

A.4 Boosting the Decay Spectrum

We now describe the general procedure to obtain the boosted spectrum from the decay spectrum at rest.

We consider a particle of mass m which decays into a number of daughter particles, and we assume that the kinematic distribution of the decay is known in the rest frame of the particle. Our goal is to determine the kinematic distribution in the lab frame, where the parent particle is moving. We take the parent particle to be traveling along the z-axis, with an energy E_m, corresponding to a Lorentz factor $\gamma = E_m/m$. We assume that there is no correlation between the direction of the daughter particle's momentum and the direction of the parent particle's boost.

In the CM frame, the four-momentum of one of the daughter particles is $(E', p' \sin\theta', 0, p' \cos\theta')$. We are given dP/dE' in the CM frame; i.e. the probability of obtaining in the CM frame a given value of the daughter particle's energy. In the lab frame, the four-momentum is $(E, p \sin\theta, 0, p \cos\theta)$. We are looking for dP/dE.

For the daughter particle in the lab frame, we have

$$E = \gamma(E' + p'\beta \cos\theta). \tag{A.26}$$

For any given E, this equation has a solution for $\cos\theta$ if E' lies in the range

$$\gamma(E - p\beta) \leq E' \leq \gamma(E + p\beta). \tag{A.27}$$

The kinematic distribution of the daughter particle in the laboratory frame is then

$$\begin{aligned}\frac{dP(E)}{dE} &= \frac{1}{2}\int dE'\ d\cos\theta \frac{dP(E')}{dE'}\delta\left(E-\gamma(E'+\beta p'\cos\theta)\right), \\ &= \frac{1}{2}\int_{E_1}^{E_2} dE' \frac{dP(E')}{dE'}\frac{1}{p'\beta\gamma},\end{aligned} \tag{A.28}$$

where $E_2 = \gamma(E + p\beta)$ and $E_1 = \gamma(E - p\beta)$. This formula allows us to obtain the boosted spectrum from the decay spectrum at rest.

If we assume that the parent particle itself has a kinematic distribution in the laboratory frame given by dN_m/dE_m, we then find

$$\frac{dP(E)}{dE} = \frac{1}{2}\int dE_m \frac{dN_m}{dE_m}\int_{E_1(E_m)}^{E_2(E_m)} dE' \frac{dP(E')}{dE'}\frac{1}{p'\beta\gamma}. \tag{A.29}$$

Moreover, if the daughter particle itself decays isotropically to some tertiary product, one can determine kinematic distribution of this tertiary product by simply repeating the above process, treating the daughter particle now as the parent to the tertiary particle.

We can apply this formalism to the case of the π^0, whose dominant decay is to two photons. In the rest frame, the photons have back-to-back momenta and the distribution is $dP/dE' = 2\delta(E' - \frac{m_\pi}{2})$, where the factor of two accounts for the two photons. We then find

$$\begin{aligned}\frac{dP}{dE} &= \int_{E\gamma(1-\beta)}^{E\gamma(1+\beta)} dE'\delta\left(E'-\frac{m_\pi}{2}\right)\frac{1}{E'\beta\gamma} \\ &= \frac{2}{\sqrt{E_\pi^2 - m_\pi^2}} \times \left[\theta\left(E - \frac{m_\pi}{2}\sqrt{\frac{1-\beta}{1+\beta}}\right)\theta\left(\frac{m_\pi}{2}\sqrt{\frac{1+\beta}{1-\beta}} - E\right)\right]\end{aligned} \tag{A.30}$$

This reproduces the usual box distribution.

If the π^0 injection spectrum is given by dN_π/dE_π, then we may express the photon spectrum as [37]

$$\frac{dN_\gamma}{dE_\gamma} = \int_{\frac{m_\pi}{2}(\frac{2E_\gamma}{m_\pi}+\frac{m_\pi}{2E_\gamma})}^{\infty} dE_\pi \left[\frac{dN_\pi}{dE_\pi}\frac{2}{\sqrt{E_\pi^2 - m_\pi^2}}\right] \tag{A.31}$$

This implies that the photon spectrum is log-symmetric about $m_\pi/2$ with a global maximum at that point. Moreover, the spectrum decreases monotonically as the energy either increases or decreases away from $m_\pi/2$. We see these features in Figure 2.1.

The last thing which is needed is dN_π/dE_π. This can be determined from the procedure described above, treating the π^0 as the daughter produced by the decay of K_L, K_S, $K^\pm$, $\rho^\pm$ and ω. But there is one subtlety to note. This approach is strictly valid only if there is no correlation between the pion boost and the boost of the parent. This is necessarily true if the parent is spin-0, but need not be true if the parent is a vector meson. But we will assume that this effect is negligible, and ignore it henceforth.

Appendix B

The Axial Portal Appendix

B.1 Chiral Lagrangian Technical Details

At lowest order, the relevant terms in the Lagrangian are the following contact interactions.

$$\mathcal{L}^{(2)}_{\text{contact}} = \frac{\sqrt{2}}{3}\alpha_{du}\beta a_\mu \left[\pi^0\pi^-\partial_\mu\pi^+ + \pi^+\pi^0\partial_\mu\pi^- - 2\pi^+\pi^-\partial_\mu\pi^0\right] \tag{B.1}$$

$$- \frac{\alpha_{du}\beta^3}{15\sqrt{2}} a_\mu(\pi^0)^2 \left[\pi^0\pi^-\partial_\mu\pi^+ + \pi^+\pi^0\partial_\mu\pi^- - 2\pi^+\pi^-\partial_\mu\pi^0\right] \tag{B.2}$$

$$- \frac{\sqrt{2}}{15}\alpha_{du}\beta^3 a_\mu\pi^-\pi^+ \left[\pi^0\pi^-\partial_\mu\pi^+ + \pi^+\pi^0\partial_\mu\pi^- - 2\pi^+\pi^-\partial_\mu\pi^0\right] \tag{B.3}$$

Now, we decompose the $\mathcal{O}(p^4)$ Lagrangian $\mathcal{L}^{(4)}_{\text{contact}}$ as

$$\mathcal{L}^{(4)}_{\text{contact}} = \mathcal{L}^{(4)}_{0+-} + \mathcal{L}^{(4)}_{000} + \mathcal{L}^{(4)}_{000+-} + \mathcal{L}^{(4)}_{0++--} \tag{B.4}$$

Expanding the chiral Lagrangian into its mesonic fields we obtain corrections to the $\pi^0\pi^+\pi^-$, $\pi^0\pi^+\pi^-\pi^+\pi^-, \pi^0\pi^0\pi^0\pi^+\pi^-$ processes and the lowest order contribution to the $\pi^0\pi^0\pi^0$ vertex.

$$\mathcal{L}^{(4)}_{0+-} = \frac{\alpha_{du}\beta^3}{\sqrt{2}} L_9 \partial_\nu a_\mu \Big[\pi^-\partial_\mu\pi^0\partial_\nu\pi^+ + \pi^+\partial_\mu\pi^0\partial_\nu\pi^- - \pi^+\partial_\mu\pi^-\partial_\nu\pi^0 - \pi^-\partial_\mu\pi^+\partial_\nu\pi^0\Big] + \mu \leftrightarrow \nu \tag{B.5}$$

$$\mathcal{L}_{000} = \sqrt{2}\beta^3\alpha_{du}\left(2L_1 + 2L_2 + L_3\right)\partial_\mu\pi^0\partial_\nu\pi^0\Big(a_\mu\partial_\nu\pi^0 + a_\nu\partial_\mu\pi^0\Big) \tag{B.6}$$

$$\mathcal{L}^{(4)}_{000+-} = \frac{\alpha_{du}\beta^5}{6\sqrt{2}} a_\mu \Big[4\left(2L_1 + L_2 + L_3\right)\pi_0\pi^-\partial_\mu\pi^+\left(\partial_\nu\pi_0\right)^2 + 4\left(2L_1 + L_2 + L_3\right)\pi_0\pi^+\partial_\mu\pi^-\left(\partial_\nu\pi_0\right)^2 \tag{B.7}$$

$$- 12\left(2L_1 + 2L_2 + L_3\right)\pi^-\pi^+\partial_\mu\pi_0\left(\partial_\nu\pi_0\right)^2 - 4L_2(\pi^0)^2\partial_\mu\pi^+\partial_\nu\pi^-\partial_\nu\pi_0 - 4L_2(\pi^0)^2\partial_\mu\pi^-\partial_\nu\pi^+\partial_\nu\pi_0 \tag{B.8}$$

$$+ 4\left(2L_1 + 3L_2 + L_3\right)\pi_0\pi^-\partial_\mu\pi_0\partial_\nu\pi^+\partial_\nu\pi_0 + 4\left(2L_1 + 3L_2 + L_3\right)\pi_0\pi^+\partial_\mu\pi_0\partial_\nu\pi^-\partial_\nu\pi_0 \tag{B.9}$$

$$- 4\left(2L_1 + L_3\right)(\pi^0)^2\partial_\mu\pi_0\partial_\nu\pi^-\partial_\nu\pi^+\Big] + \mu \leftrightarrow \nu \tag{B.10}$$

$$\mathcal{L}^{(4)}_{0++--} = \frac{\alpha_{du}\beta^5}{3\sqrt{2}} a_\mu \Big[(2L_1 + L_3) \left(\pi^+\right)^2 \partial_\mu \pi^0 \left(\partial_\nu \pi^-\right)^2 + 4L_2 \pi^0 \pi^+ \partial_\mu \pi^+ \left(\partial_\nu \pi^-\right)^2 + 2L_2 \left(\pi^+\right)^2 \partial_\mu \pi^- \partial_\nu \pi^0 \partial_\nu \pi^- \tag{B.11}$$

$$+ 4 (2L_1 + L_2 + L_3) \pi^0 \pi^- \partial_\mu \pi^+ \partial_\nu \pi^+ \partial_\nu \pi^- + 4 (2L_1 + L_2 + L_3) \pi^0 \pi^+ \partial_\mu \pi^- \partial_\nu \pi^+ \partial_\nu \pi^- \tag{B.12}$$

$$- 10 L_2 \pi^- \pi^+ \partial_\mu \pi^+ \partial_\nu \pi^0 \partial_\nu \pi^- - 10 (2L_1 + L_3) \pi^- \pi^+ \partial_\mu \pi^0 \partial_\nu \pi^+ \partial_\nu \pi^- + 2L_2 \left(\pi^-\right)^2 \partial_\mu \pi^+ \partial_\nu \pi^0 \partial_\nu \pi^+ \tag{B.13}$$

$$+ (2L_1 + L_3) \left(\pi^-\right)^2 \partial_\mu \pi^0 \left(\partial_\nu \pi^+\right)^2 + 4L_2 \pi^0 \pi^- \partial_\mu \pi^- \left(\partial_\nu \pi^+\right)^2 - 10 L_2 \pi^- \pi^+ \partial_\mu \pi^- \partial_\nu \pi^0 \partial_\nu \pi^+ \Big] + \mu \leftrightarrow \nu. \tag{B.14}$$

Throughout this paper, we make use of the definitions

$$\alpha_{ij} = \alpha_i - \alpha_j \qquad \text{for} \qquad i, j \in \{u, d, s\} \tag{B.15}$$

$$\beta = \frac{\sqrt{2}}{f}. \tag{B.16}$$